

# Team 3D Final Design Report

---

22 April 2014

Scott Ashcraft (GT)  
Ignacio Jose Benitez Cruz (PU)  
Nicolaus Caniza (PU)  
Tanveer Chandok (GT)  
Roman Esteban Hofer (PU)  
Aaron Inouye (BYU)  
Michael Kelley (PU)  
Stephen Lutgring (PU)  
Michael Miles (BYU)  
Jean Ruggiero (PU)



## Abstract

As a multi-university collaborative project sponsored by The Boeing Company and supported by Stratays, students from Purdue University, Georgia Tech, and Brigham Young University designed and built a blended wing Unmanned Aerial System (UAS) for the purposes of obtaining aerial imaging (NDVI and visible) of agricultural fields in an effort to improve the efficiencies of farming (i.e., providing current data of the soil and plant conditions rather than bi-annual or quarterly data). This report contains the aeronautical engineering methods used to iteratively design and manufacture a fused deposition modeled (FDM) UAS. In the process of designing, extensive preliminary analyses, experimental testing, and numerical analyses were performed. The engineering software primarily used entails the following: XFLYR5, AVL, MotoCalc, Star CCM+ (CD Adapco), and ANSYS Workbench.

## Basic Aircraft Configuration

The final aircraft design consists of a 3D printed airframe as shown in the system walk-around in Figure 1. The system is launched using a catapult launcher with bungees to achieve the required take-off velocity. Elevon control surfaces provide pitch and roll control while winglets provide yaw stability and serve to reduce induced drag. One AXI 4130/16 electric motor fitted with a 16x8" composite propeller in a tractor configuration provides thrust for the aircraft. A payload module sits along the aircraft centerline and includes the avionics required for flight, the Tetracam ADC Lite NDVI imager, and flight batteries.

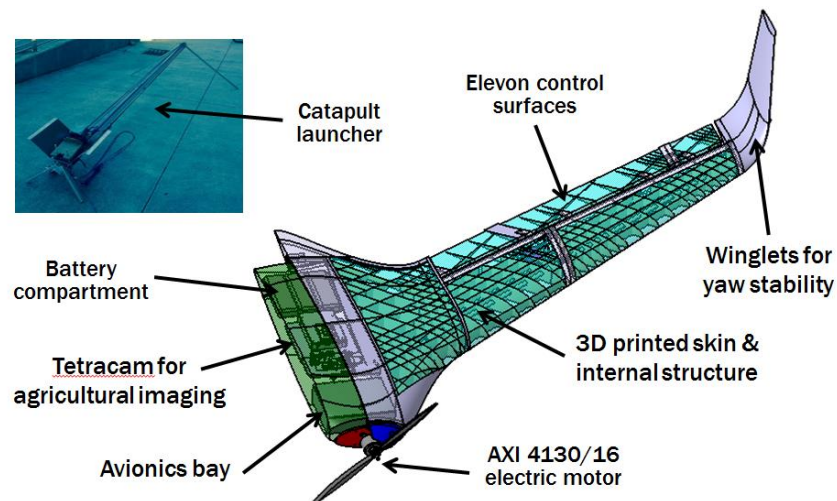


**Figure 1:** System walk-around

The three-view drawing given in Figure 2 shows the overall dimensions of the aircraft. The aircraft has a wingspan of 89.5 inches and an aspect ratio of 7.1. The total wing area is 7.83 ft<sup>2</sup>. The gross weight is 11.7 pounds, just shy of the maximum weight of 12 pounds listed in the request for proposals.

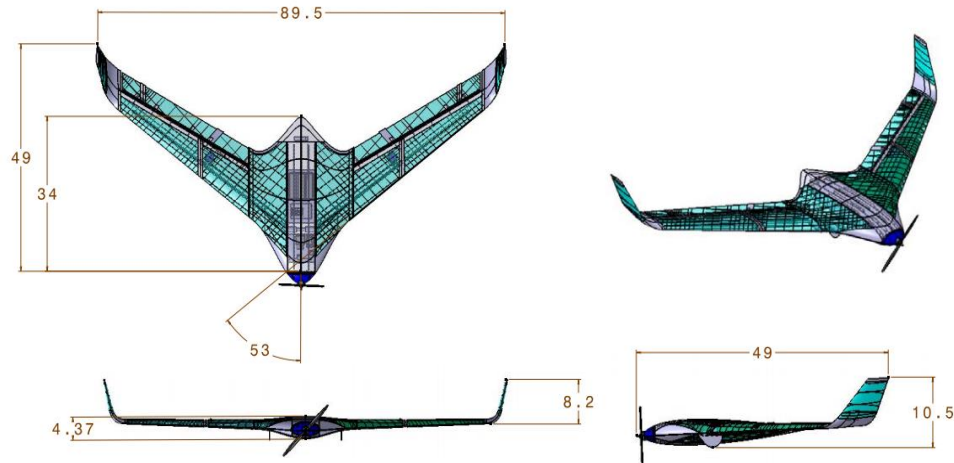


**Figure 2:** Three-view of final aircraft design

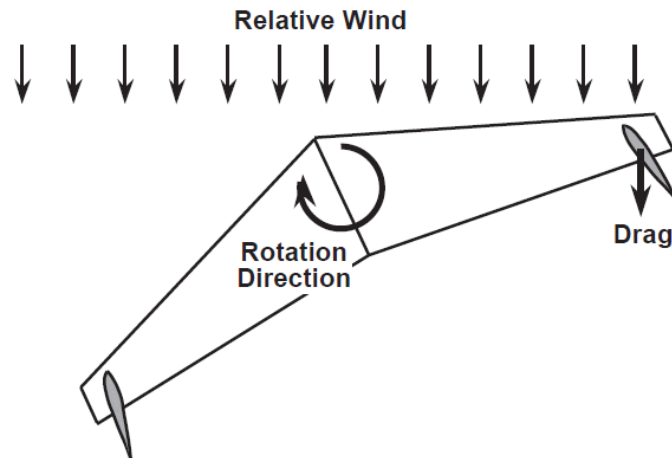
## Detailed Design

### Aerodynamic Design

During the conceptual design phase, the aircraft planform, wing span, wing sweep, wing aspect ratio and airfoil sections were selected, making the basis for further aerodynamic analysis. The aerodynamics analysis during the preliminary and detailed design consisted of a trade study to determine the optimal vertical stabilizer configuration, sizing of winglets, and a Computational Fluid Dynamics (CFD) analysis.

**Stabilizer Configuration.** Yaw stability on a flying wing aircraft is harder to achieve compared with a conventional tailed aircraft. Adding a vertical tail is the simplest way to add yaw stability. Two vertical stabilizer configurations were considered and analyzed: twin tail and winglets. First, a theoretical investigation was performed in order to determine the aerodynamic performance of each configuration.

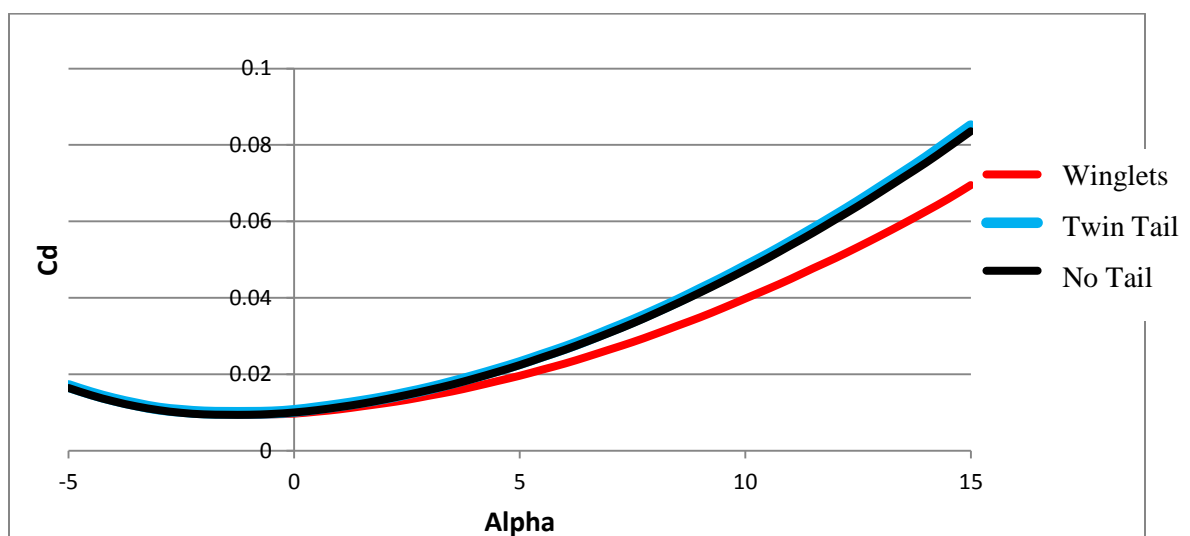
Winglets increase the aspect ratio of a wing without materially increasing the wingspan. The intended effect of winglets is to reduce the aircraft's drag by decreasing the trailing vortices at the wing tips, improving lift to drag ratio. The yaw stability can be increased by giving the winglets some "toe-in" or "toe-out" angle, as shown in Figure 5, since it allows the flying wing to rotate back to the intended direction of flight. When the flying wing experiences a yawing moment, as shown in Figure 3, the winglet that is forward presents more of its profile to the wind, and thus creates a more drag than normal while the opposite winglet experiences less drag than normal. The resulting force imbalance creates a yawing moment about the center- of-gravity that turns the glider back into its intended direction of flight.



**Figure 3:** Restoring force caused by toe-in angle

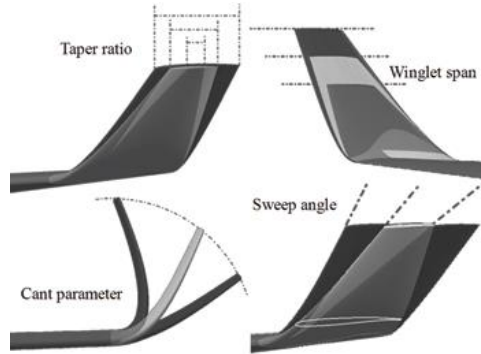
A disadvantage of winglets is that they add weight far behind the axis of symmetry of the wing, causing higher root bending moments. To allow for the increased bending moment, increasing the strength and thus the weight of the wing may be necessary. This disadvantage can be solved by situating the vertical stabilizers closer to the axis of symmetry. The vertical stabilizers would act now as a twin tail instead of winglets. However, not only would the benefit of reducing drag disappear; a drag penalty when compared with a completely tailless aircraft would exist. In the case of a twin tail configuration, the distance from the stabilizers to the center of gravity is smaller and therefore there is a smaller moment arm (compared to the winglets), reducing the effective yawing moment and reducing the yaw stability of the aircraft. To increase the moment arm to the center of gravity, the twin tail can be mounted on two longitudinal booms. This would lead to a more complex structure and additional and more complex structural analysis would have to be performed.

Figure 4 shows the drag of the baseline aircraft, the aircraft with the winglet configuration, and the aircraft with the twin tail configuration. From an aerodynamic standpoint, the winglet configuration is the most effective.



**Figure 4:** Drag results for investigated stabilizer configurations

**Winglet Sizing.** An aerodynamic analysis was performed using XFLR5 to size the winglets such that the aerodynamic performance of the aircraft is maximized. The design parameters that were taken into account can be seen in Figure 5 below. The impact of each parameter was studied while maintaining the others constant.



**Figure 5:** Design parameters for winglet

Figures 8, 9, and 10 show the effects of the cant angle, winglet span, and winglet sweep angle on the lift to drag ratio ( $L/D$ ) of the aircraft. In Figure 6, it can be seen that increasing the cant angle increases the maximum lift to drag ratio. However, increasing the cant angle reduces the projected area of the winglet, thus reducing the yaw stability of the aircraft. Therefore the cant angle will have to be iterated to find the optimum compromise between aerodynamic performance and stability.

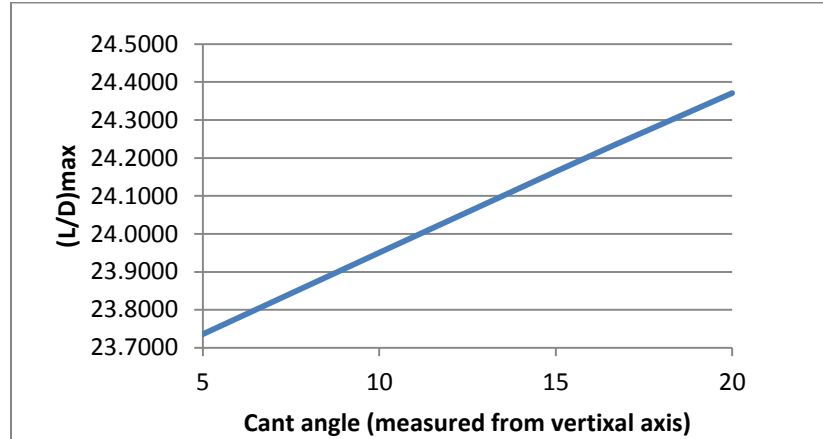


**Figure 6:** Cant angle vs. maximum lift to drag ratio

In Figures 7 and 8, the effect of the winglet span and the sweep angle, respectively, can be seen. It can be seen from these figures that there is an optimal value of each of these two parameters that will result in the highest maximum lift to drag ratio.

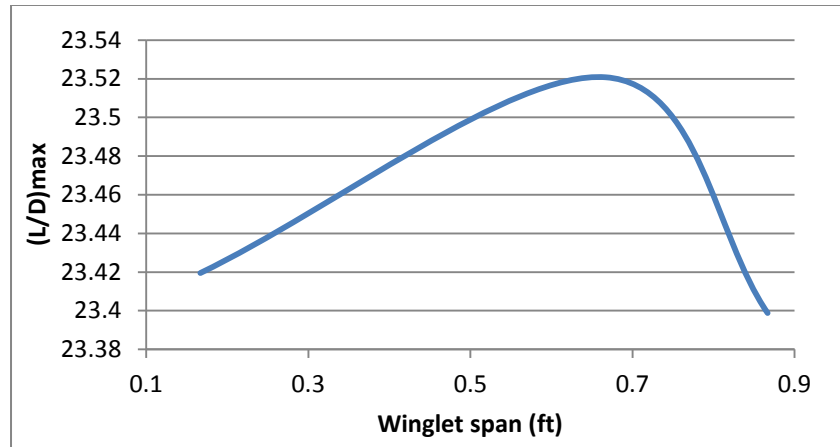


**Figure 7:** Winglet span vs. maximum lift to drag ratio

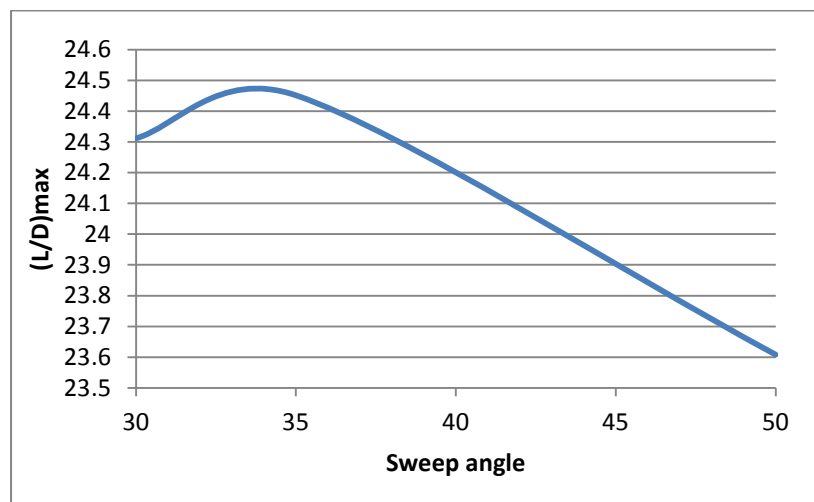


**Figure 8:** Sweep angle vs. maximum lift to drag ratio

The optimal combination of these design parameters leads to the improvement shown in Figure 9. A cant angle of 15 degrees, winglet span of 0.67 ft, and winglet sweep angle of 34 degrees were selected. One can see from Figure 11 that winglets improve the aerodynamic performance over that of the baseline aircraft. The winglets lead to an improvement of the aerodynamic performance (maximum lift to drag ratio) of 5.82%.

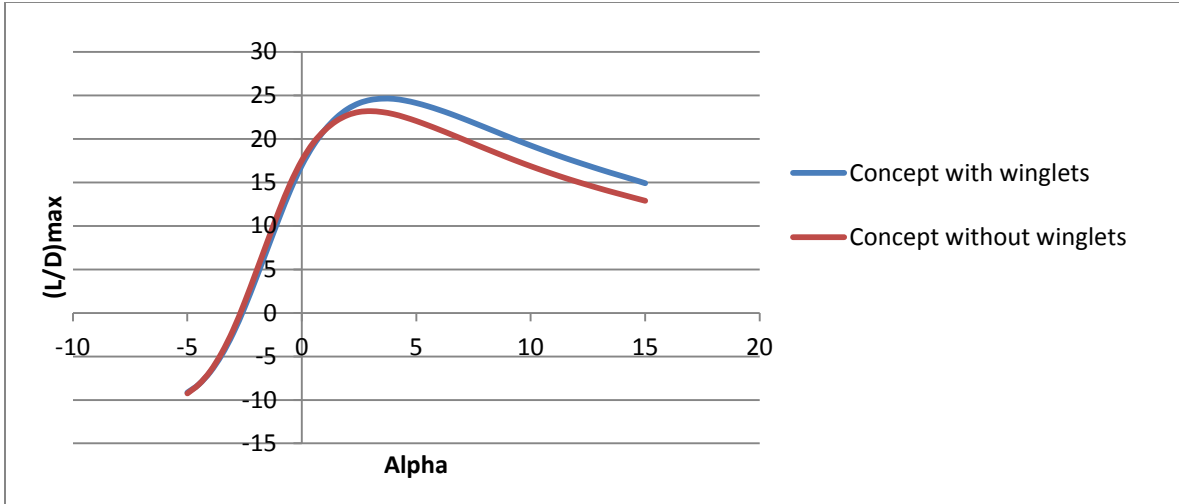


**Figure 9:** Comparison of concept with and without winglets

## Structural Design

The structural analysis of the aircraft design consisted of research regarding typical structural layouts and selection of a structural layout and construction method. Numerous steps were taken to analyze the available options. Materials analysis was performed to choose the optimal material for the aircraft. Preliminary structural analyses were performed in AVL and XFLR5, though the final tests were done in ANSYS 13.0. Plans for a structural test of a 3D printed wing segment were laid out and proposed CAD models were created for these parts.

**Material Selection.** In order to select materials for use in the construction of the aircraft, performance indices for bending and shear loads were calculated and plotted on an Ashby chart. By plotting the performance indices on an Ashby chart and checking the intersection points, one can establish materials that maximize strength in bending and shear loads while minimizing density.

The weight of a structural element is given by

$$W = \rho AL$$

where  $W$  is the weight of the element,  $\rho$  is the material density,  $A$  the cross-sectional area of the element, and  $L$  the element length. The bending stress experienced by a structural element is given by

$$\sigma = \frac{-My}{I}$$

where  $\sigma$  is the bending stress,  $M$  is the moment imposed on the element,  $y$  is the moment arm, and  $I$  is the moment of inertia of the element cross section. Fixing geometry and combining weight and bending stress relations gives the performance index for bending:

$$P_{CR} = \frac{\sqrt{\sigma}}{\rho}$$

Similarly, the performance index for shear force can be determined by considering the relation for shear force:

$$\tau = \frac{P}{A}$$

where  $\tau$  is the shear stress experienced by a structural element,  $P$  is force imposed by a point load, and  $A$  is the cross-sectional area of the element. Combining this relation with that for the weight of the structural element and again fixing geometry gives the performance index for shear:

$$P_{CR} = \frac{\sigma}{\rho}$$

These performance indices for both bending and shear were then plotted on an Ashby chart with the appropriate axes as shown in Figure 10. The blue lines represent the shear performance index and the red lines represent the bending performance index. These lines intersect at the locations circled in green. The purple circle in Figure 10 shows the location of 3D printed materials on the Ashby chart. From the Ashby chart, it can be seen that the best suited materials for this application are engineering ceramics, engineering composites, and 3D printed materials

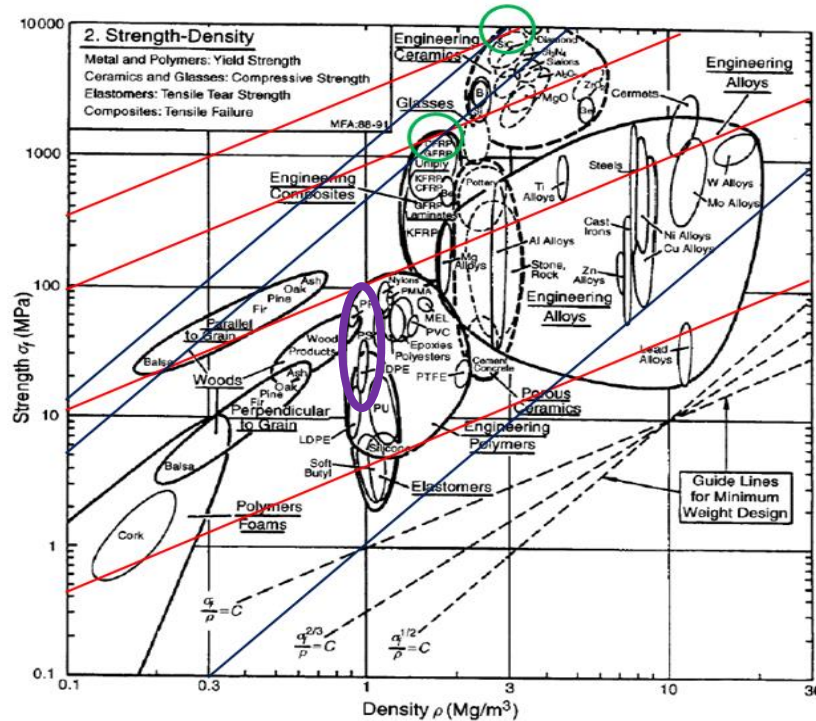


**Figure 10:** Plot used for Ashby material selection process

Once the material choices were narrowed down using the Ashby material selection process, a cost versus strength trade was performed to further narrow down the list. Figure 11 shows a plot of strength versus cost for several common materials. It can be seen from Figure 11 that composites are strong but expensive and so should be limited to use in high stress areas, such as spars. In addition, it can be seen that ceramics are very expensive and not applicable to the current aircraft design. Polymers, including 3D printed



material are sufficiently strong and inexpensive for this project and should be used for low loading areas including ribs and skin.

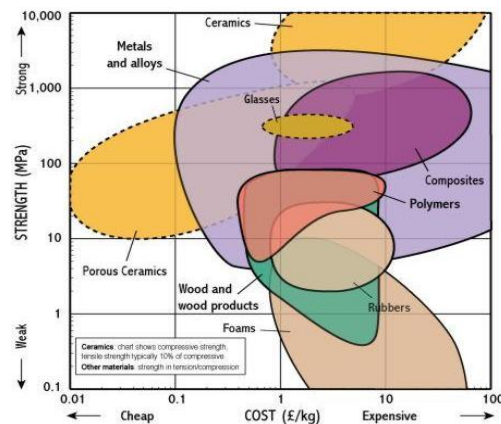


**Figure 11:** Cost vs. strength plot used for material selection

After consulting Stratasys, the specific material chosen was ABS-M30 production grade thermoplastic. ABS-M30 is up to 25 to 70 percent stronger than standard Stratasys ABS and is an ideal material for conceptual modeling, functional prototyping, manufacturing tools, and end-use-parts. ABS-M30 has greater tensile, impact, and flexural strength than standard ABS. Layer bonding is significantly stronger than that of standard ABS, leading to a more durable part.

**Structural Layout Selection.** For the fabrication breakdown, several different existing structural layout methods were examined. These methods were then weighed against each other as their pros and cons were considered. The methods considered are geodesic, traditional rib-spar, foam core, and hollow wing mold.

A geodesic design was considered since this layout helps balance structural loads in a cylindrical fuselage by including stringers that handle loads from both sides of the airplane. However, since the aircraft at hand does not have a traditional cylindrical fuselage, and is a blended wing body, this design technique adds too much complexity without providing enough benefit for it to be chosen. The traditional rib-spar design has been tried and tested successfully by many RC airplane designers. It has proven to be a good balance of simplicity and performance. However, the internal rib-spar structure can get quite complicated since cutting and assembling many wing sections would be cumbersome. Additionally, damage to a traditional rib-spar aircraft usually results in the complete loss of the airframe since the structure cannot be easily repaired. A foam core design with a fiberglass or composite skin would be the easiest to manufacture and the materials used for this technique are typically cost effective. This method often costs more weight than necessary and does not have appealing performance characteristics. Airplanes using foam structures are generally heavier than those of the same strength using the rib-spar design. Additionally, for a professionally made airplane, the materials may be expensive. The hollow wing mold method is easy for duplicating parts, but the materials used may not be strong enough for the current application. Composite materials could be used to overcome this, but this process requires very intricate manufacturing techniques including the construction of several sets of molds. Once these molds are fabricated, however, the remainder of the manufacturing process is relatively fast and easy.

The chosen technique for the final product is a rib-spar design that is optimized for a blended wing body. Using 3D printing, many of the risks of using this technique can be overcome or eliminated. The 3D printing process is very repeatable, eliminating the problem of creating multiple products with the same characteristics. Using the rib-spar design with the right materials, the structure can achieve a low overall

weight with desirable strength. After choosing a structural layout method for the aircraft, a rough rib and spar layout was drafted. Figure 12 shows a sketch of the chosen layout. Potential locations for carbon fiber spars are highlighted in green.

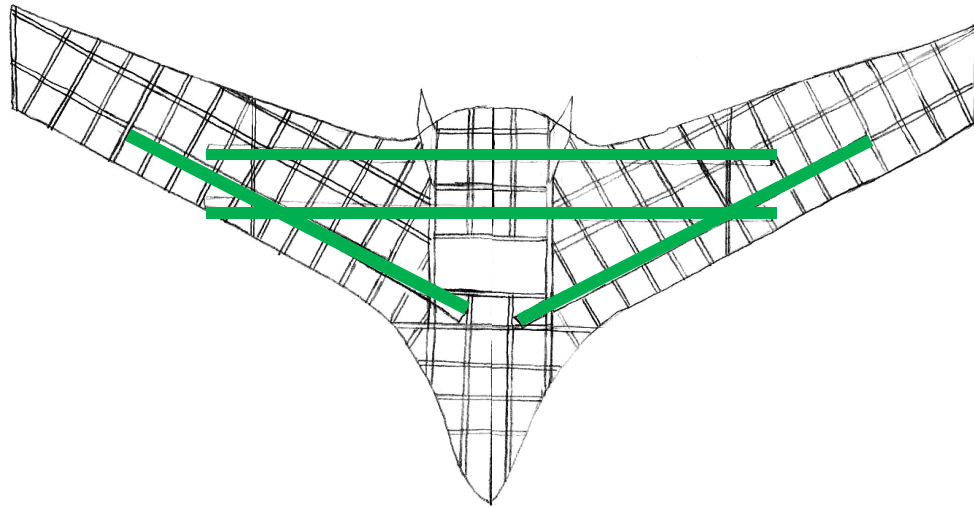


**Figure 12:** Aircraft internal structure

**AVL Structural Analysis.** A force analysis was conducted within both XFLR5 and AVL to determine the expected flight loads that the aircraft structure would experience. This analysis was conducted over a range of flight velocities and angles of attack. The results of the bending moment analysis are shown in Figure 13 below. As expected, the maximum bending moment occurs at the root of the wing on the aircraft center line. Both XFLR5 and AVL analyses are depicted for the 35 mph and 50 mph test case. Additionally, load factors of four were applied to the AVL results, as AVL calculated the highest loadings of the two software programs. This load factor accounts for the increased load to which the airframe will be subjected during turns.

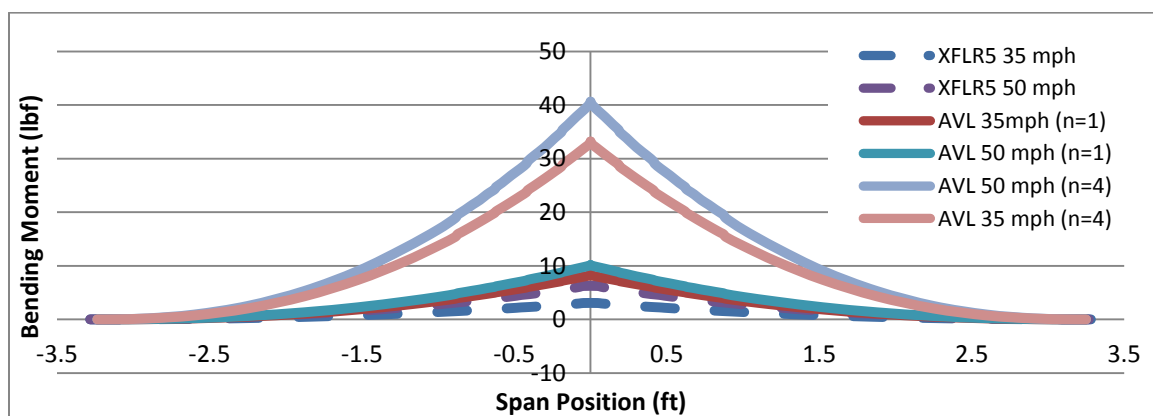


**Figure 13:** Bending moment analysis using XFLR5 and AVL

Similarly, a shear force analysis was conducted for the same flight conditions. This analysis was only conducted using AVL due to the inability to achieve reliable results with XFLR5. As can be seen from Figure 14 below, the maximum shear force calculated for the aircraft was at a flight velocity of 50 mph, resulting in a force of approximately 7.5 lbf. While this loading is significantly lower than that of the bending forces, special attention will need to be paid to ensure the 3D printed parts will be able to maintain these loads.

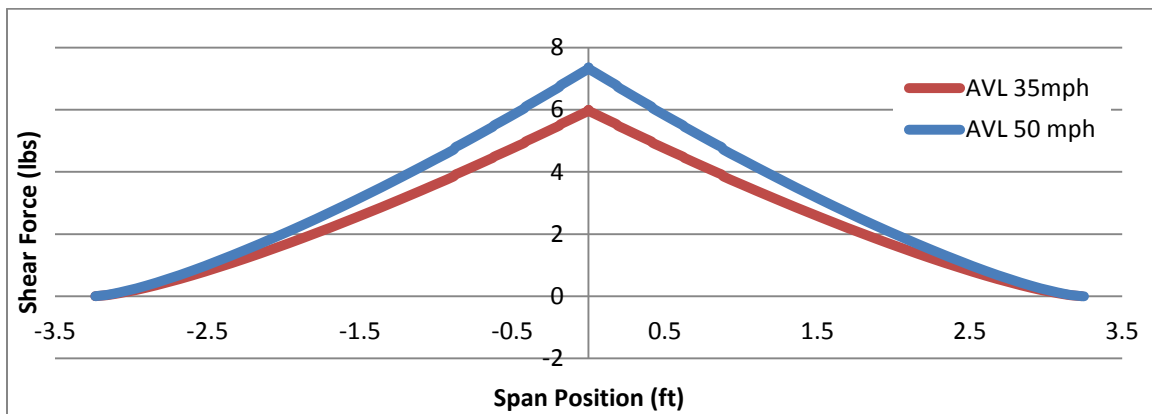


**Figure 14:** Shear analysis conducted within AVL

**Final Structural Design.** Further structural analysis and testing was used to determine the optimal number and strength of these spars. Analytic studies produced two possible layouts for the wings of the aircraft, which would then dictate the construction of the remainder of the aircraft. The primary differences between them are the thicknesses of the ABS-M30 material used for printing. The Fuse Deposition Modeling technique, pioneered by Stratasys, allowed the aircraft components to be printed in the spanwise direction for precise control of the outer mold line. The ribs and spars were designed to be printed inside the outer mold line simultaneously. The process allows the operator to control the thickness of parts down to the number of layers of material that are used in printing. Since the ribs, spars, and skin were essentially to be a single piece, loads could be easily distributed. This allowed the spacing of the ribs and spars to be determined in large part by weight constraints. Skin thickness, however, was found to be an essential test parameter due to the load it would carry.

The team decided to test a single layer and two layer skin design for the final round of testing. These were to become the 3D printed test pieces tested at Brigham Young University, detailed in structural test section, and were also the subject of the detailed FEA analysis, detailed in the FEA section. The final result of these examinations proved that the structure had suitable strength characteristics with a single layer skin. This was especially good news for the weight considerations of the aircraft. Furthermore, the carbon fiber spars tested with the ABS-M30 wings created a very stiff structure that would not deform significantly when subjected to in-flight loads.

Figure 15 shows the final structural layout of the fuselage and inboard wing section of the aircraft. The yellow planes represent components that were layer controlled during printing for a precise thickness, and include the majority of the spars and ribs. The tubes that pass through the section are the main spar tube, which held the carbon fiber spar, and a wiring tube for the control surface servos. The grey solid parts indicate components that were printed using an enclosed honeycomb structure. This honeycombing technique creates the strength and appearance of a solid block, but is significantly lighter due to the empty space. The exact honeycomb shapes are determined automatically by the 3D printers, allowing the designers to simply create solid objects in CAD programs.

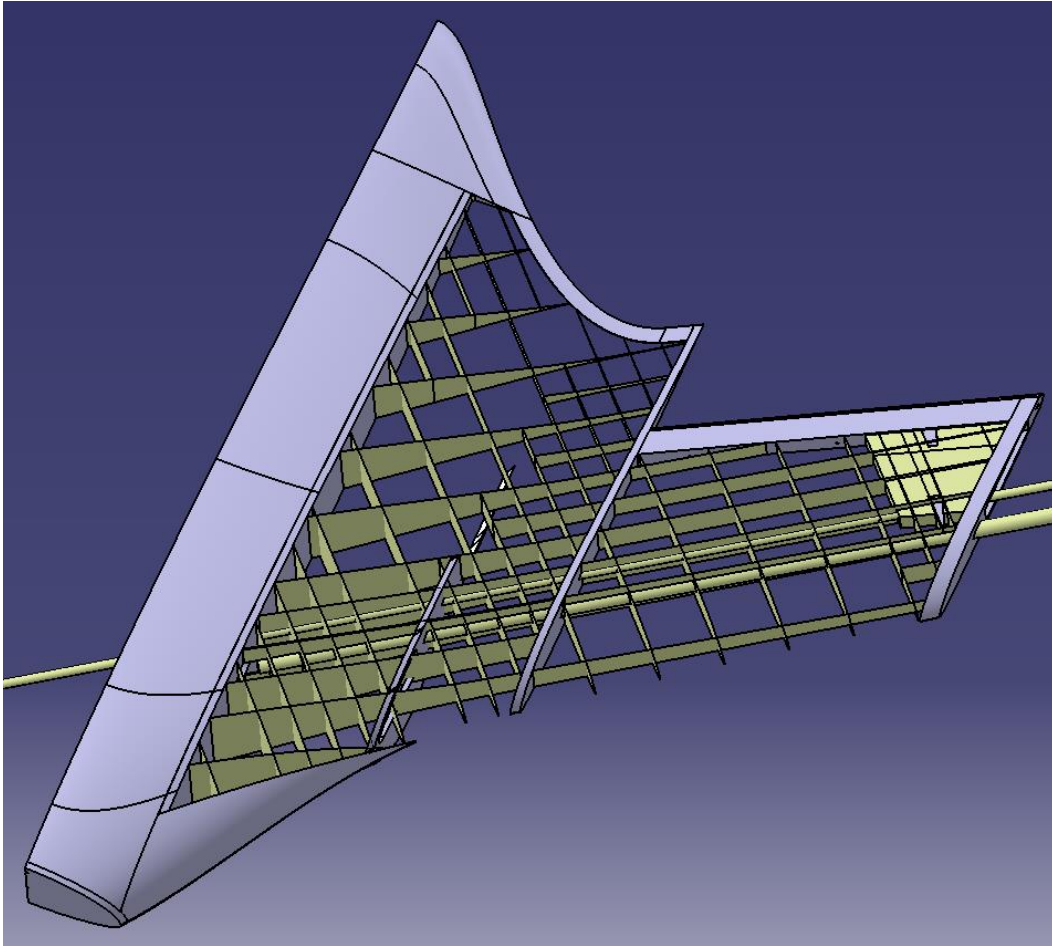


**Figure 15:** Fuselage and wing blending section without skin

## Propulsion System

A propulsion system analysis was performed in order to determine the optimal combination of motor, propeller, and batteries for the specific application at hand. The system was selected using MotoCalc and analyzed to determine its performance. The initial system was designed to launch off of a catapult and fly an aircraft weighing 8 lbs, based on estimations of the weight of 3D printed sections. However, the final aircraft was overweight by 4 lbs, leading to a rolling cart launch method. There was a clear need for a more powerful propulsion system to get the aircraft to take-off, since the initial propulsion design did not consider a ground roll. This section describes the initial propulsion system followed by a comparison to the final propulsion system.

**System Selection.** The initial propulsion system was selected using MotoCalc. Specifically, a subprogram of MotoCalc called Motowizard was used to narrow down the initial selection of propulsion systems. Motowizard uses several inputs such as airfoil shape, planform size, mission type, and weight to select the best propulsion combination from a stored catalog of parts. The three best propulsion systems selected by Motowizard were further analyzed to confirm the Motowizard selection. First the propeller size was analyzed for each of the propulsion systems. Figure 16, Figure 17, and Table 1 show the analysis for the Hacker A40-12S propulsion system. Figure 16 shows the revolutions per minute (RPM) of the propeller versus the motor power for several propeller sizes. Figure 17 shows the RPM of the propeller versus the propulsion thrust for several propeller sizes.

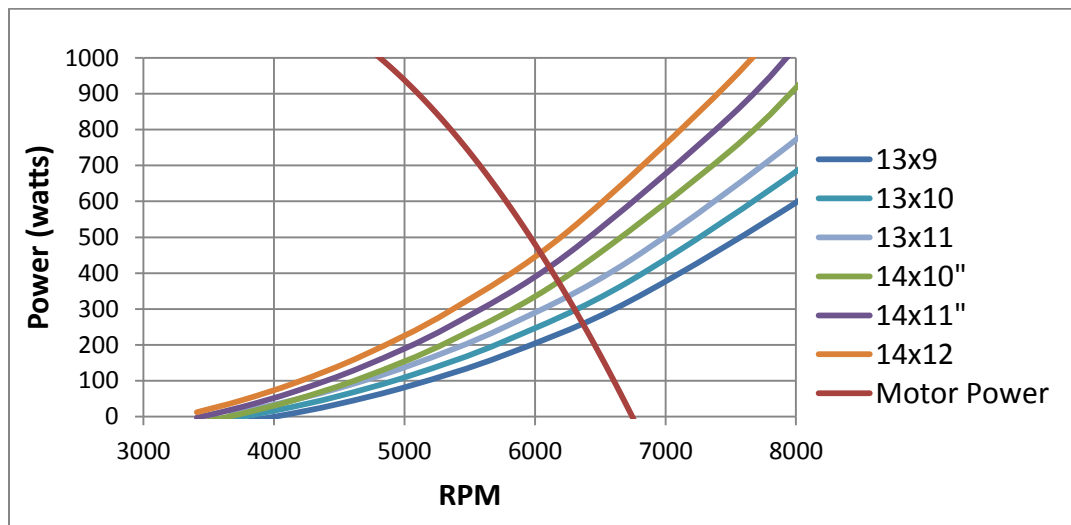


**Figure 16: Power vs. propeller RPM**

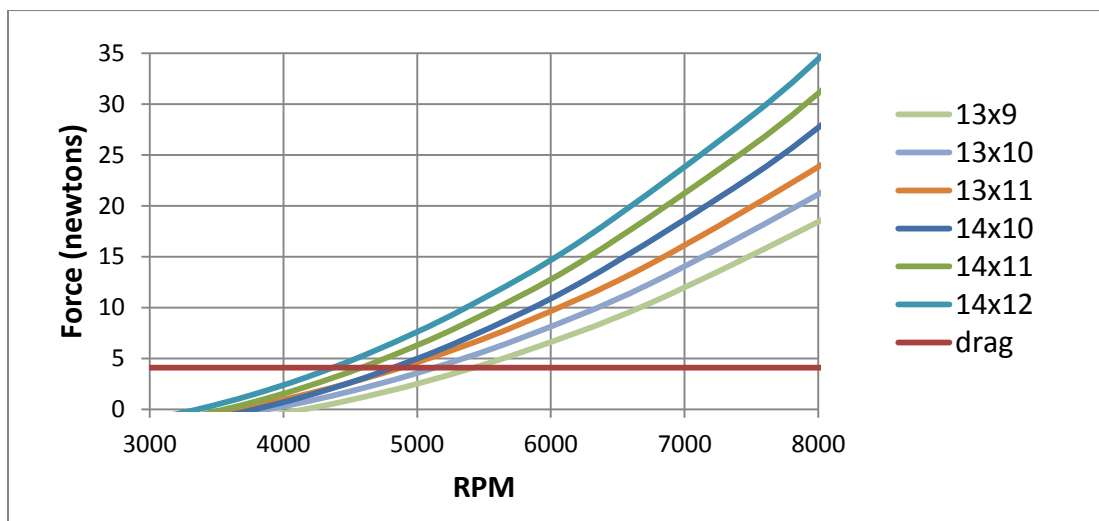


**Figure 17: Thrust vs. propeller RPM**

As can be seen in Figures 16 and 17, as the propeller size increases, the total power and thrust of the propulsion system increase. However as the propeller size increases, the risk for propeller stall also increases. Table 1 shows the propeller stall speed for several propellers and that a propeller size of 14x10 inches minimizes the chance for a propeller stall at takeoff while maximizing propulsion thrust and power.

**Table 1:** Propeller Stall Speed

Propeller Size (in)	Aircraft Speed (mph)
13x9	0
13x10	8
13x11	14
14x10	4
14x11	10
14x12	15
14x13	20

**System Performance.** After confirming that the selections made by MotoCalc were viable, the performance of the complete propulsion systems was compared. Figure 18 shows a graph of efficiency and propulsion system thrust to weight ratio versus air speed for each of the three top propulsion systems.

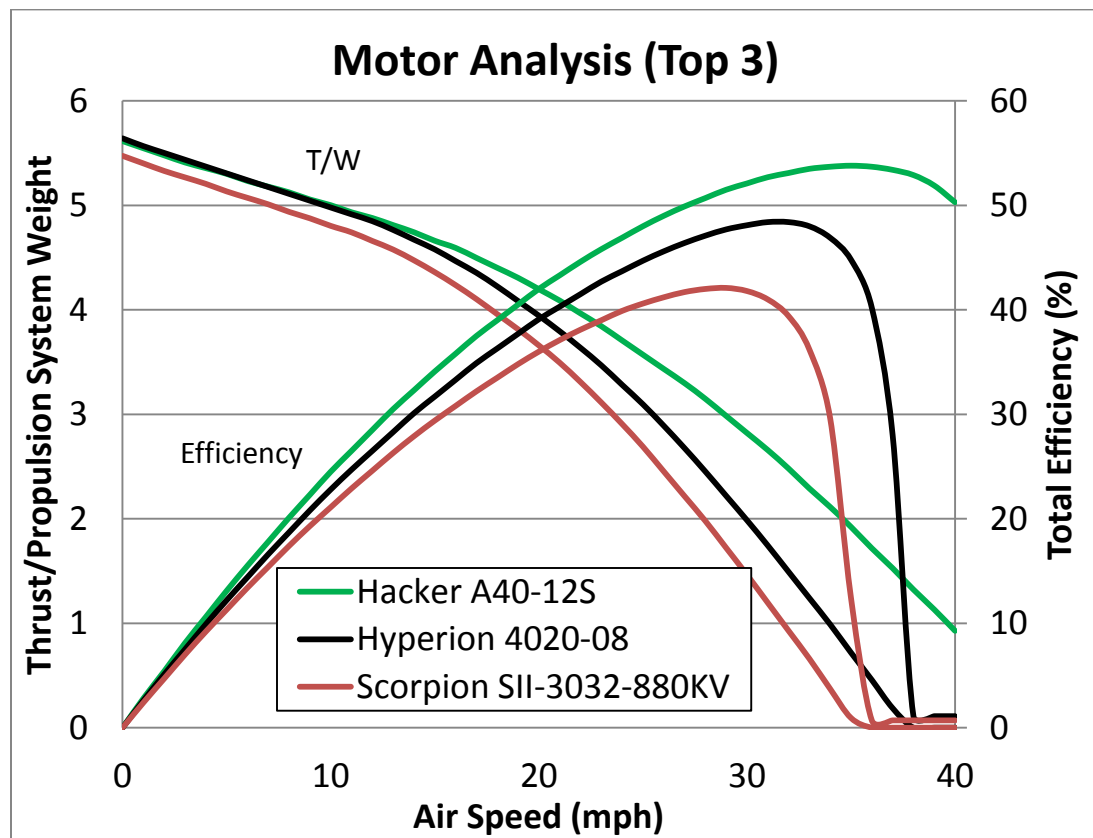


**Figure 18:** Non-dimensional thrust and efficiency versus flight speed

As can be seen in Figure 18, the Hacker A40-12S propulsion system provided the most thrust and the best efficiency of the three propulsion systems. This data matched the Motowizard output which listed the Hacker A40-12S propulsion system as the best propulsion combination for the aircraft. The Hacker A40-12S system was therefore selected. Specifically, the system includes the Hacker A40-12S version two motor. The selected propeller is 14x10 inches in size. The battery system will consist of three lithium polymer battery backs connected in parallel. Each of the battery packs consists of three lithium polymer battery cells connected in series. Each battery pack produces 11.1 volts and has four ampere-hours of

charge. The propulsion system will have a total efficiency of 55% at cruise. The propulsion system will provide a thrust to weight ratio of 0.087 for the aircraft.

The Hacker A40-12S system was eventually replaced due to take-off concerns. The new propulsion system, while less efficient at cruise, will provide significantly more thrust at take-off. Table 2 shows a comparison of the initial and final propulsion systems. As can be seen by Table 2, the final configuration will allow the aircraft to take off in nearly half of the distance as the initial Hacker A40-12S system.

**Table 2: Propulsion System Comparison**

	<b>Initial Configuration</b>	<b>Final Configuration</b>
<b>Motor</b>	Hacker A40-12S	AXI 4130/16
<b>Battery</b>	LiPo 3S-3P (20C)	LiPo 6S-1P (50C)
<b>Propeller</b>	14x10"	15x8"
<b>Static Thrust</b>	5 lbs	8.6 lbs
<b>Estimated Take-Off Distance</b>	145 ft.	85 ft.

## Stability & Control

The stability of the aircraft was a cause of concern throughout the design process because of the inherent instability of tailless aircraft. Athena Vortex Lattice (AVL) was used to analyze the aircraft design and determine its characteristics in pitch stability. AVL was used to size the elevon control surfaces and determine the deflections needed to keep the aircraft stable at different flight points. Wind tunnel testing was then performed to determine the aircraft pitching moment as a function of angle of attack using the  $\frac{3}{4}$  scale prototype. The test data was compared to data from AVL in order to validate the model. Figure 19 shows the raw test data in dark blue. This is the pitching moment about the point on the aircraft connected to the wind tunnel mounts. The light blue curve is a fit curve to the raw test data. The black points show the moment coefficient about the aircraft center of gravity as calculated from the test data and the green curve shows the corresponding AVL results. One can see that the test results match the AVL results closely and thus the AVL model provided an adequate representation of the actual system.

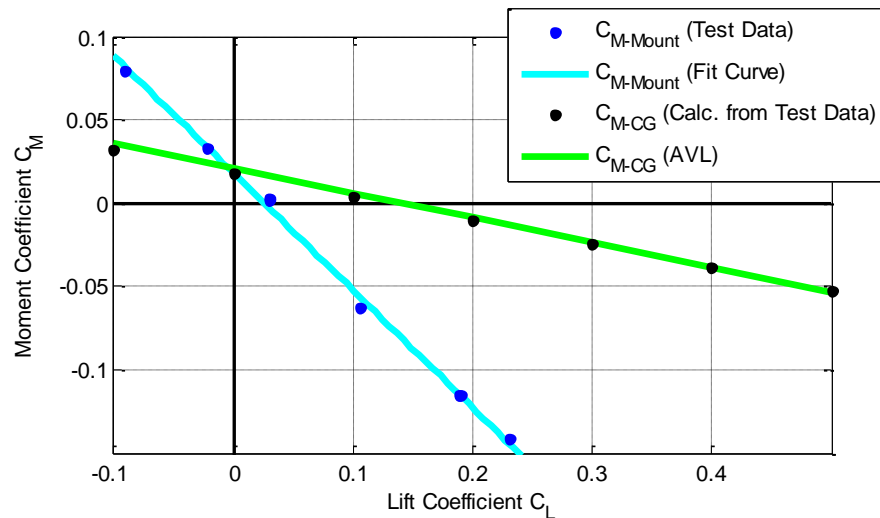


**Figure 19: Pitching moment data from wind tunnel & AVL**



## Weight & Balance

A weight and balance analysis was performed in order to determine where components need to be located in order to achieve the desired center of gravity on the final aircraft. The initial analysis was done using an Excel spreadsheet to determine the center of gravity based on all of the component weights, sizes, and locations. An initial component layout was then created and used to complete the CAD models. The initial estimate turned out to be a little off since the center of gravity of the airframe was simply estimated at that point. The printed parts came out heavier than anticipated and it was not until after the aircraft was assembled that the center of gravity of the structure could be determined by hand. Once the aircraft was fully assembled with all components, the batteries were moved and the center of gravity of the entire system checked by hand until the desired location was achieved.

The location of the center of gravity was determined by first choosing a desired static margin. A static margin of 15% was chosen. The static margin of a traditional tailed aircraft is usually selected to be in the range of 5% to 10% but a slightly higher static margin is often selected for tailless aircraft due to their inherent pitch instability. The location of the center of gravity is related to the static margin by:

$$SM = \frac{AC - CG}{MAC}$$

where  $SM$  is the static margin of the aircraft,  $AC$  is the location of the aerodynamic center measured aft of the nose,  $CG$  is the location of the center of gravity measured aft of the nose, and  $MAC$  is the mean aerodynamic chord length. The final design has an aerodynamic center located 26 inches aft of the nose and a mean aerodynamic chord of 17.08 inches. For a static margin of 15%, the center of gravity is to be located 23.44 inches aft of the aircraft nose.

## Avionics & Sensors

The avionics system was selected by balancing cost, weight and engineering requirements. In addition, compatibility with the propulsion and other aircraft systems were considered during the selection process. Specifically a speed controller, autopilot and radio controller were selected.

**Speed Controller Selection.** The Castle Phoenix Edge 60 HV speed controller was selected because of its maximum amperage and voltage cutoff ability. The selected propulsion system can draw a maximum of 50 amperes from the battery. The selected speed controller allows a maximum current draw of 60 amperes which provides a safety margin of 10 amperes. In addition the Castle Phoenix Edge 60 HV will cut off the voltage drawn from the battery, at a user specified amount, which will prevent damage to the lithium polymer battery cells.

**Autopilot and Controller Selection.** ArduPilot and the Spectrum DX5e Radio Controller were selected to control the aircraft as autopilot and controller, respectively. ArduPilot was selected because of its ease of use to program and operate. In addition, several team members have experience using the autopilot system which will allow for a small learning curve. The ArduPilot system is also relatively inexpensive with a cost of just \$240. Finally, ArduPilot includes a GPS and the software to operate the system is open source freeware with an active user community of 46,000 members. The aircraft will be flown at cruise using the ArduPilot. To assist in takeoff and landings the Spectrum DX5e radio controller and corresponding receiver were selected. The radio is simple to use and includes five radio channels (one for throttle and four for control surfaces) that operate at a frequency of 2.4 GHz. Figure 20 is a wiring diagram of the electrical subsystems described above.



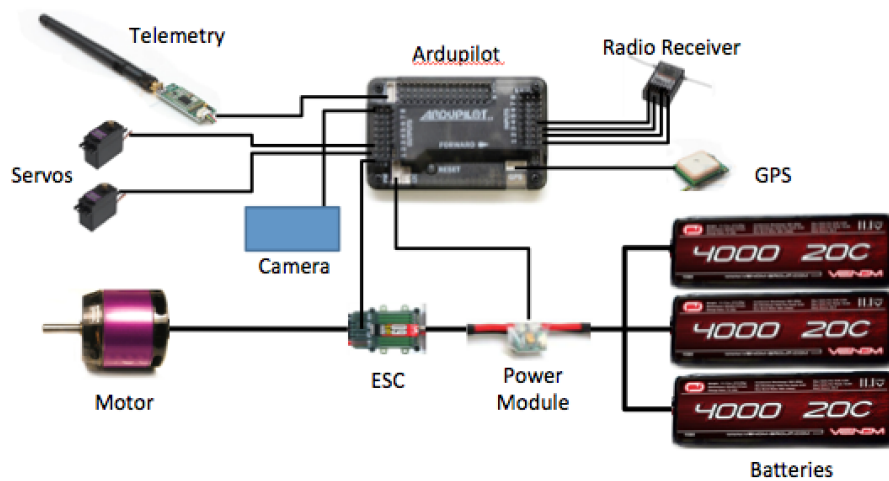


**Figure 20:** Wiring layout of payload bay and avionics

## Launcher Design

After analyzing the finalized aircraft design, it was decided that some sort of launching mechanism was required. Due to the aircraft's wingspan, weight and propeller size, a traditional hand launch would have not been viable. Furthermore, the scope of this project is to build a UAS for agricultural purposes, with minimal user interaction. Under these conditions, it was assumed that the user would not know how to hand launch a UAS and there would be no runway for traditional take-offs. After these assumptions and restrictions were applied, it was decided that a collapsible, contained and repeatable launch system would be needed.

After scanning the online forums, a design for a catapult launcher (used for the X-8 Skywalker RC airplane) was found. Since the launcher was intended for use with a smaller size airplane, the designs found online had to be modified so that the launcher would be able to provide enough thrust and stability for the UAS being designed. One of the team members on Team 3D (Scott Ashcraft) had significant experience with this type of launcher and had written up a research paper on its modified use for larger airplanes. Using this knowledge, the following design requirements were applied for the launcher:

- Maximum length: 10 feet (collapsible into two 5-foot components for storage & transport)
- Take-off speed of at least 30 feet/second for a 12-lbs airplane

Figures 21 and 22 shows the original X-8 catapult launcher design obtained from the RC groups website (see bibliography for details). This launcher is 6.5 feet long, and the bungees provide tension of 40 lbs. At this size, the launcher is not adequate for the use with the UAS being developed.



**Figure 21:** X-8 catapult launcher



**Figure 22:** X-8 catapult launcher with aircraft

Figure 23 below shows the main rail section of the launcher that was built. The main rail consists of 2 separate 5-foot 2"x2" beams of aluminum joined together using latches (Figure 24).



**Figure 23:** Modified launcher - main rail



**Figure 24:** Latches used to secure the main rail

The main rail was supported by leg extension supports at either end. The rear supports were  $\frac{1}{2}$ " x  $\frac{1}{2}$ " tubes of aluminum, while the front supports were 2"x1" tubes. Bulkier material was used for the front legs to that they did not buckle under the immense force during launch. The front legs were reinforced using a cross beam. These parts can be seen in Figure 25.

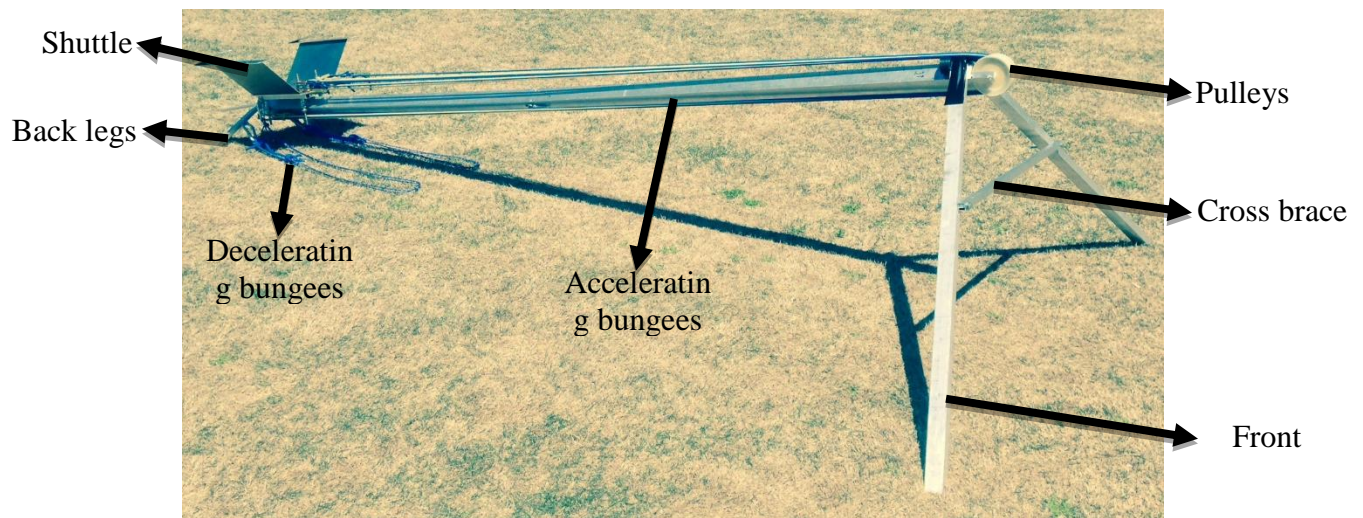


**Figure 25:** Completed Launcher

The shuttle (as seen in Figure 25), rides on top of a carriage system. The carriage system consists of 4 ball bearings (2 on each side) that ride along the main rail. The steel shuttle plate (used since it is a lot more rigid than aluminum) was bolted onto the carriage assembly. Two arms on top of the shuttle hold the aircraft in place.

To provide a sufficient launch force, accelerating bungees were used (as seen in Figure 25). Four bungees were used on each side of the carriage (total of 8 bungees). These bungees were attached using carabineers (easy to take off/add more bungees). The bungees extended from the base of the shuttle, to the front of the launcher, around the pulley system and back to the shuttle. Each of the 8 bungees was 6-feet long at 300% elongation and provided 10 lbs of force. The entire system of bungees provided 80 lbs of force (double of what was used for the X-8 catapult launcher). To decelerate the shuttle and prevent it from hitting the front of the launcher with immense force, decelerating bungees were used. These bungees

were tied to ropes so that they would only be used after the shuttle was halfway down the main rail. This ensured that the launcher would not wear itself out after only a few launches. This also helped transfer the forces from the shuttle to the decelerating bungees instead of the main rail.

Using high speed cameras, it was determined that the bungee catapult launch system had a velocity of ~35 ft/sec while carrying a 12-lbs load. This was sufficient to launch the UAS being designed by Team 3D.

### **CFD Analysis**

A CFD analysis was performed using CD Adapco's Star CCM+ software to confirm and validate the XFLR5 results obtained during the conceptual design phase and the wind tunnel test. The CFD analysis consisted of the validation of three different angles of attack 0, 2.5 and 6.3 degrees at a velocity of 30 mph.

For the CFD simulation, the following conditions were approximated: segregated flow, incompressible flow, turbulent regime, and the K-Omega turbulence model was used. In order to complete the mesh, an iterative approach was followed by starting with a coarse mesh, then confirming that everything is correct and making adjustments and afterwards performing a more refined mesh from the previous analyses. The mesh used for the CFD analysis consisted of a prism layer close to the surface of the aircraft to aid in capturing the boundary layer than will form there. Capturing the boundary layer is critical to obtaining accurate skin friction drag results as well as obtaining the correct results when varying the angle of attack. The meshing model chosen for the analyses was the trimmer mesh, which with the grid lines aligned with the flow provides an efficient approach to getting valid results. The disadvantage of the trimmer mesh is that when changing the angle of attack the cells will have to be aligned to the flow and therefore a new mesh will have to be generated for the different angles of attack. To align the cells with the flow a trimmer wake refinement was performed on the wing. This provided a more refined mesh at the wing and at the wake and allowed as well to align the cells with the flow.

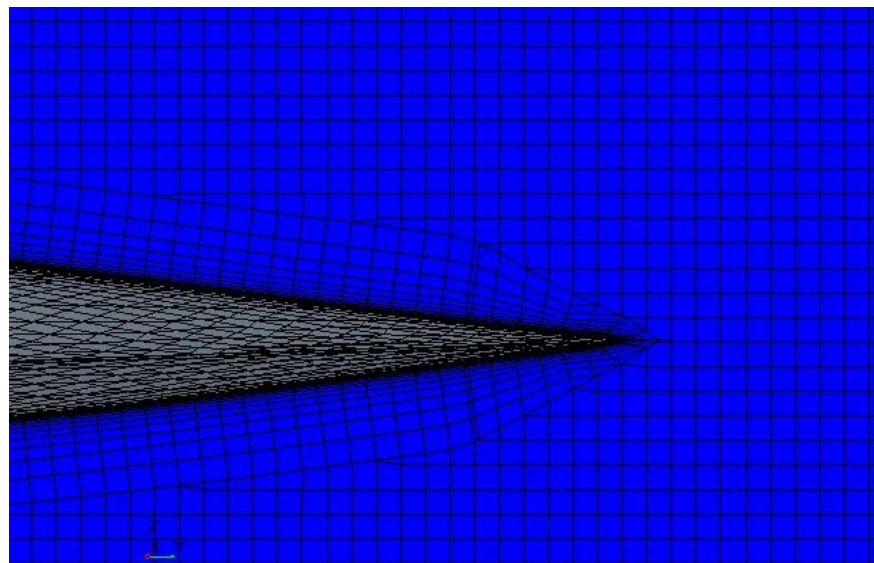


**Figure 26:** Image of Prism layer meshing (trailing edge)



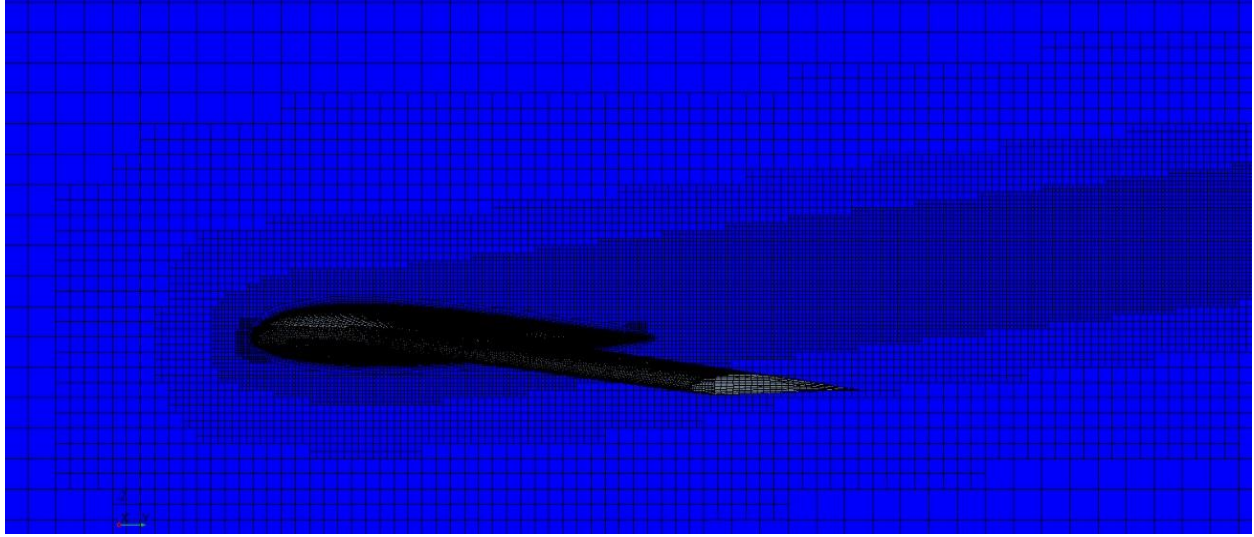


**Figure 27:** Trimmer wake refinement aligned with flow

To analyze the different angles of attack the flow direction had to be changed in the boundary conditions and the lift and drag coefficient were aligned perpendicular and parallel respectively to the flow. The following figures show the comparison of the results of XFLR5, STAR CCM+ and the Wind tunnel for a range of angles of attack from 0 to 8.5 degrees.

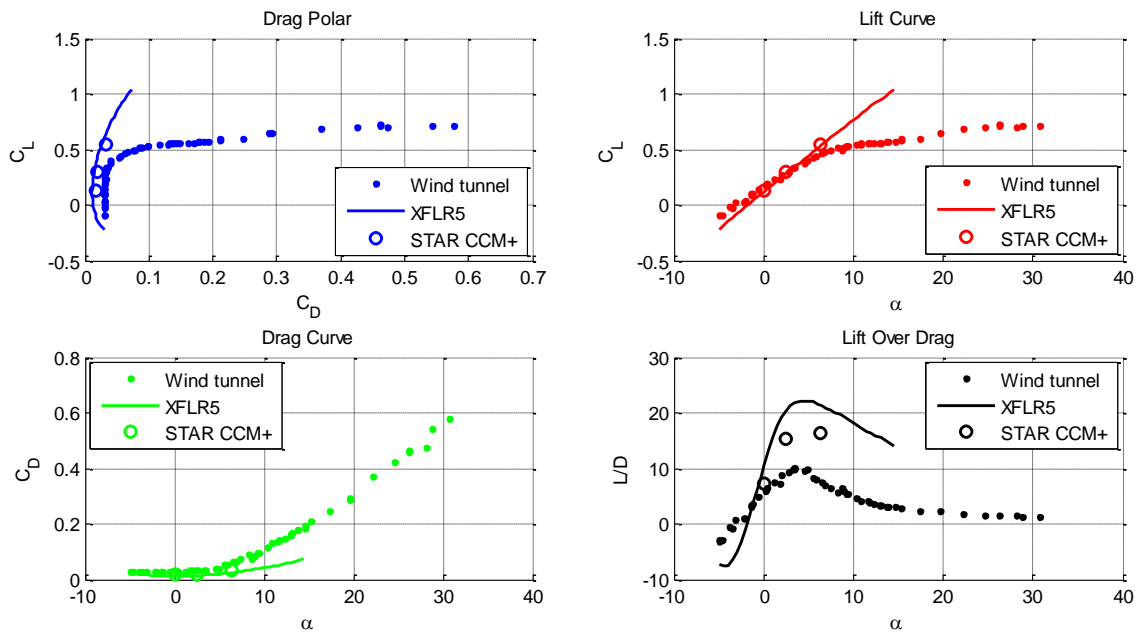


**Figure 27:** Comparison of wind tunnel, CFD, and XFLR5 aerodynamic data

From Figure 27, it is shown that Star CCM+ and XFLR5 underestimate the drag compared to the wind tunnel results. Nevertheless Star CCM+ has a better prediction in computing the drag than XFLR5. This is due the reason that XFLR5 has limitations in predicting the wingtip vortices which increase the induced drag. Figure 27 shows that Star CCM+ and XFLR5 predictions for the lift coefficient are very close but overestimated compared to the result in the wind tunnel.

There are several explanations as to why the Star CCM+ results do not match the results from the wind tunnel. Sources of error include the prototype tested in the wind tunnel had the motor installed, the control horns and rods, the hatch was not perfectly aligned with the body, the winglets were two plates attached perpendicular to the wingtip and the prototype was exerted to some yaw when mounted on the supports in the wind tunnel. All these imperfections guide to an increase in interference and excrescence drag compared to the smooth model used for the analyses in Star CCM+.

The below figures contain flow visualizations from Star CCM+ for two different angles of attack.

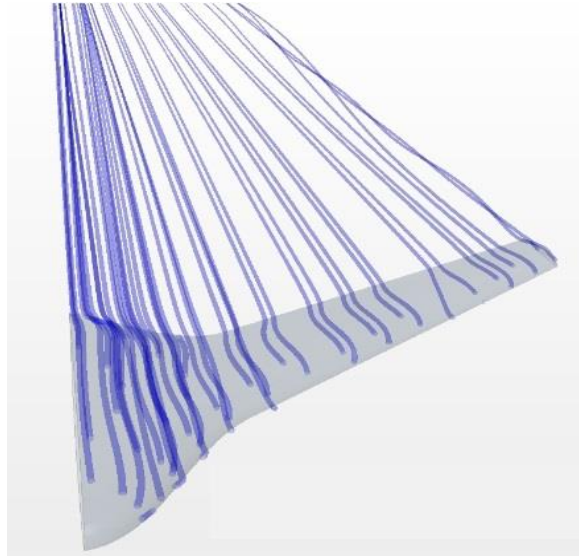


**Figure 28:** Flow visualization for an angle of attack of 0 degrees

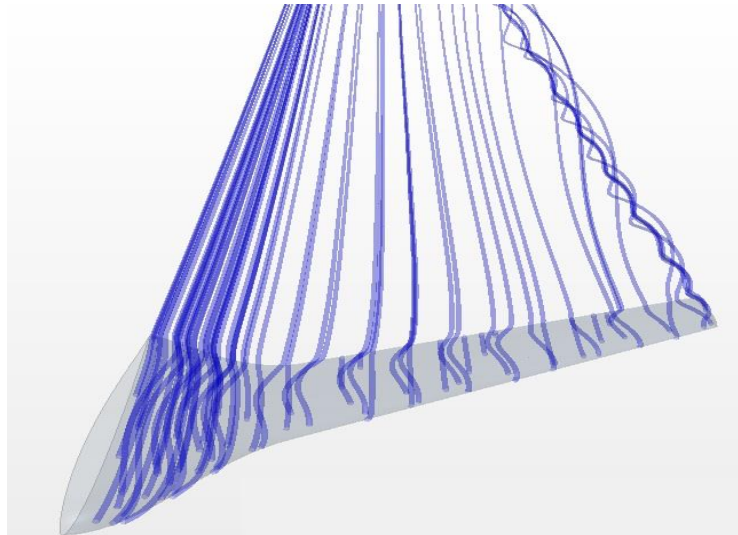


**Figure 29:** Flow visualization for an angle of attack of 6.3 degrees

It can be observed that for an angle of attack of 0 degrees, the flow stays aligned in the direction of the incoming flow while in the case of 6.3 degrees the flow starts heading in the span wise direction. Another remarkable difference is that the wingtip vortices caused for the higher angle of attack are more entangled causing higher induced drag.

## FEA Analysis

Finite Element Analysis (FEA) is an essential component to aircraft design. It provides a method for predicting the performance of the aircraft structure in expected flight regimes and survivability in the event of unexpected departures from planned flight. Due to the unusual nature of the aircraft construction, computer generated finite element modeling (FEM) was essential to complete the FEA. The program used was *ANSYS 13.0 Workbench, Student Edition*, which is the software made available to students at Purdue University.

The reduced capacity of the student edition of ANSYS created certain difficulties unique to this project. The large number of components in the aircraft design, made necessary by the use of light weight and thin 3D printed materials, meant the entire aircraft could not be analyzed at once. It was decided the best use of the FEA process would be to replicate the experimental testing conducted on sample wing sections at Brigham Young University. This would provide two comparable models of how the 3D printed ABS-M30 structure could handle in flight stresses and, most importantly, help determine the issue of how thick the aircraft skin needed to be.

**FEM.** The first step to the analysis is creating the finite element model. This was done using CAD models of the aircraft wing section in question. Although original plans called for using the exact models of the test sections that were printed for experimentation, this proved to be infeasible due to the honeycombed solid structures that were included to mount and apply loads to the test parts. While these components of the structure were modeled as solids in CAD, they are printed as a low density honeycomb in order to save material and weight. This could not be replicated in the FEM, and would later prove to be detrimental to the modeling of fuselage components as well. The replacement model was that of the actual wing section that was designed for the aircraft. Since the test wing was intended from the beginning to accurately simulate the real wing (all internal structures and outer mold lines were the same), this was not deemed to be a significant concern.

Due to the nature of the modeling process required for 3D printing on FDM equipment, all of the surfaces in the CAD model were originally created as two dimensional surfaces. In the ANSYS Workbench, it was necessary to isolate the individual components (ribs, spars, skins, etc.) and assign each one their respective thickness. The components were then “joined” together using ANSYS connection options. After the first round of ANSYS testing, it was found that a new CAD model had to be created in order to create the carbon fiber spar that would fit in the 3D printed tube of the wing.

ANSYS then breaks up the components into elements with which to do testing. The meshing process used to generate the elements proved to be another difficult task. Irregularly shaped elements can cause the software to compute load and material information in that section improperly, leading to incorrect results. While an impromptu sizing study was conducted to determine the optimal element size and shapes, the program would often crash when it deemed too many elements were in use. This contradicted reports of the number of elements that ANSYS 13.0 should be capable of handling, but was attributed as a drawback to the student edition. Screenshots of the final model, with the elements visible, are provided in the figures below.

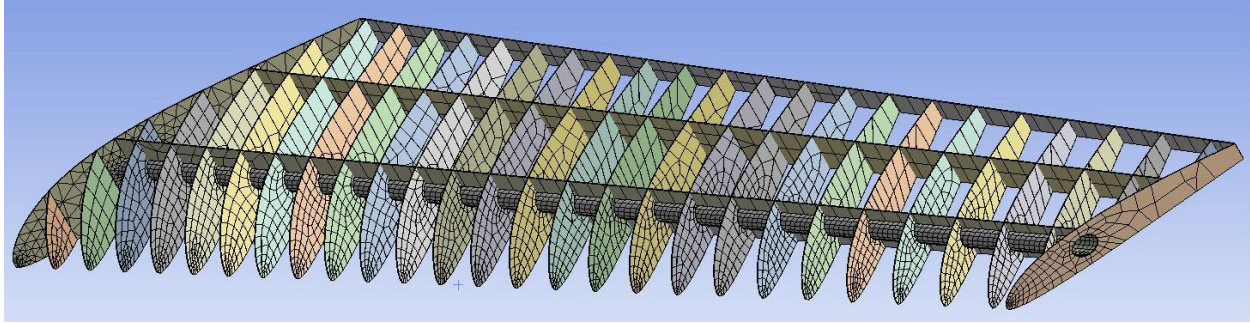


**Figure 30:** ANSYS wing model with skin hidden

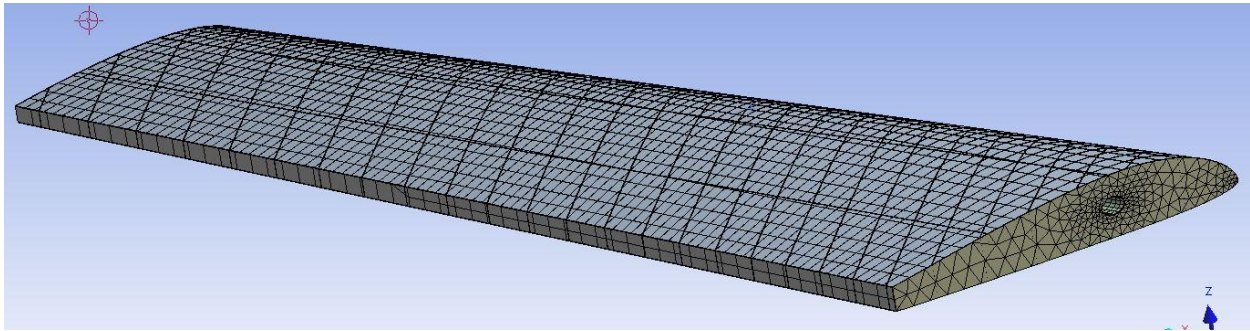


**Figure 31:** ANSYS wing model with skin visible

**Material Properties.** The second component to the FEA process is the consideration of the material properties. This proved to be the most problematic part of the process, since there has been little research on the ABS-M30 material and the Stratasys FDM printing technique. The baseline for the material properties was simply taken from the data sheets available on the Stratasys website. This information was used to complete development of the first ANSYS model, which was built only to simulate the ABS-M30 wing section. The results of this model proved to differ significantly from the experimental results. While the results predicted relatively small deflections, which is good for the design, the significantly larger deflections of the experimental tests indicated that there was a clear problem with the model.

Discussions with Stratasys engineers produced two possible solutions. The first was accounting for the way FDM printing fuses material together. While each layer of material will have a certain thickness, it is not the same as the thickness of the area across which two layers of material bond together. This “bonding thickness” can result in a 20% to 30% loss in effective material thickness when dealing with a single layer of material oriented in that direction. Unfortunately, in order to take advantage of the precision of the printers, this was the direction necessary for the aircraft parts to be printed. This is illustrated in the diagram below.



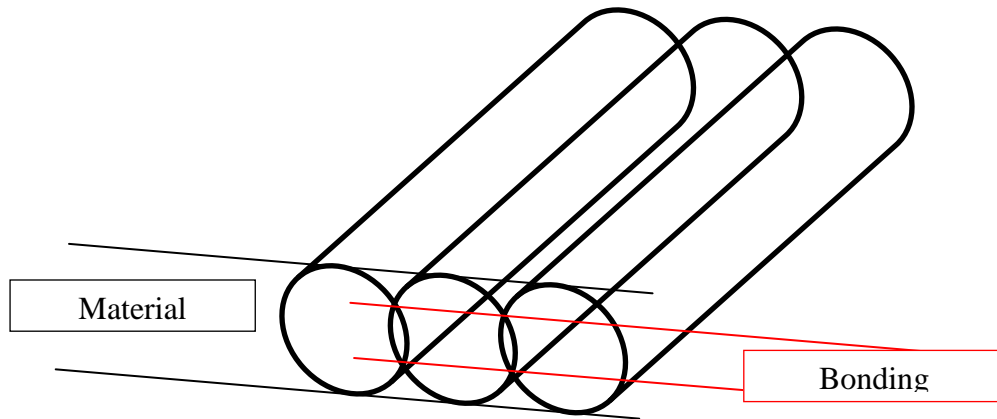


**Figure 32:** Material thickness compared to bonding thickness in a single 3D print layer

The second solution utilized an additional test that was conducted at Stratasys to attempt to analyze the change in physical properties of the ABS-M30 material when stressed in bending as described above. Three small test samples of known sizes, called coupons, were tested and loaded in bending to failure. Stress and strain information gathered during the testing was used to calculate new values of Young's Modulus to replace those from the Stratasys data sheets.

The results of all three of these analysis methods are shown in the graph below. The bonding thickness model assumed a 30% reduction in the effective thickness of all components, as well as considering a modulus of 300 ksi based on a prior recommendation from Stratasys. The model using the newest modulus information from the coupon testing assumed no reduction in the effective material thickness, but used a modulus of approximately 214 ksi (the average result of the three coupon tests). All plots are for models with a single layer skin thickness, since at this point the experimental testing had already proven it to be adequate.

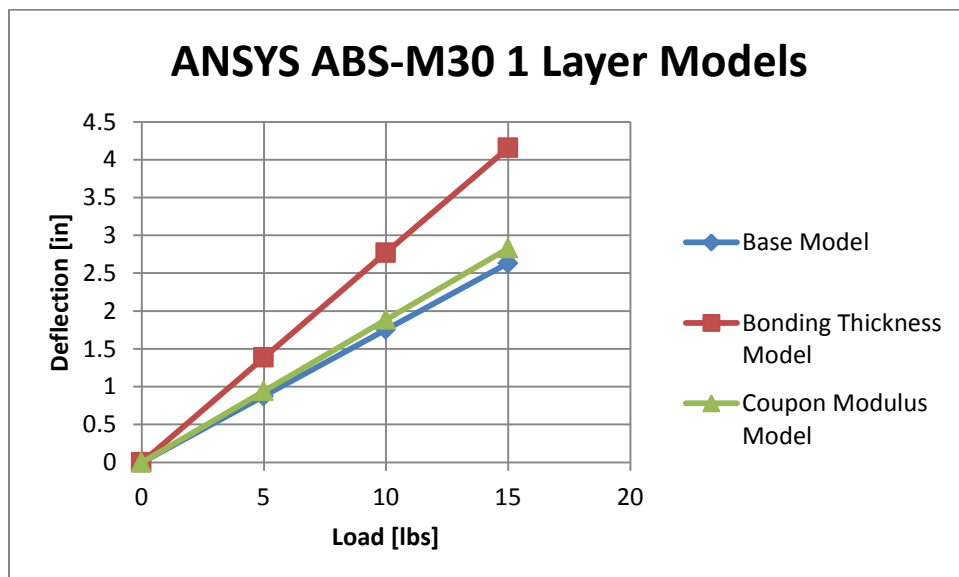


**Figure 33:** Comparison of three ANSYS models

The two new methods of modeling produced improved results in ANSYS over the original material properties. A carbon fiber spar was added to these models, as described earlier. The carbon fiber material properties were used from existing research conducted by team members at Purdue. These results are as follows.

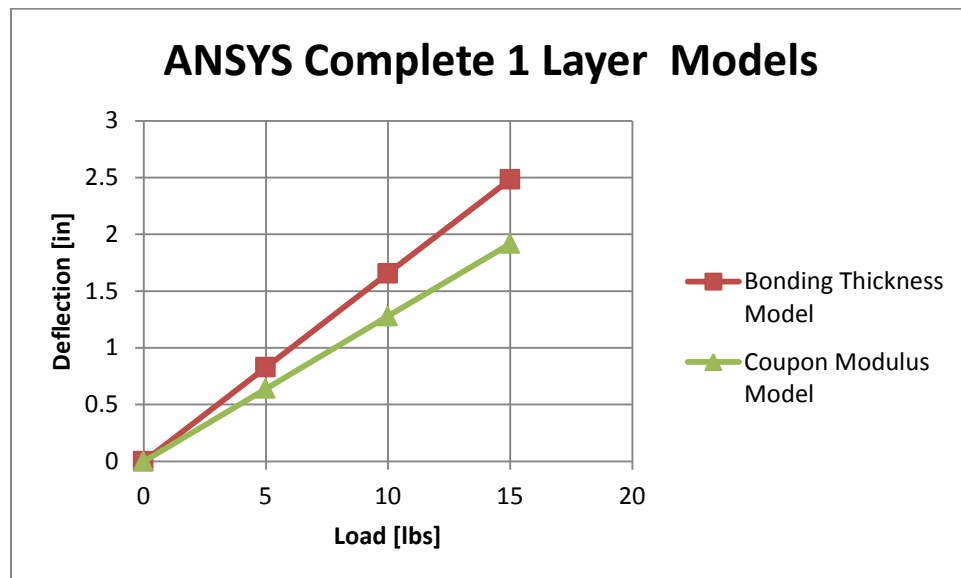


**Figure 34:** Comparison of two modified ANSYS models with carbon fiber spar included

**Final Results.** After evaluating the possible ANSYS models, the bonding thickness model was found to be closest to the experimental data. The following three graphs show the relation between this ANSYS model and the corresponding experimental testing results. Both methods were conducted on the single layer skin wings, and both with and without the carbon fiber spar in place.

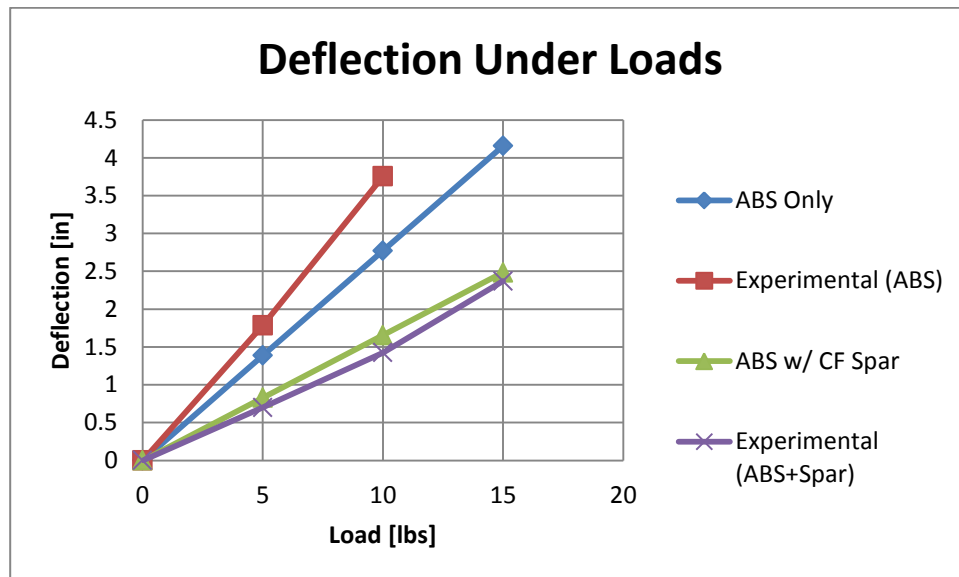


**Figure 35:** Comparison of bonding thickness ANSYS model with experimental results

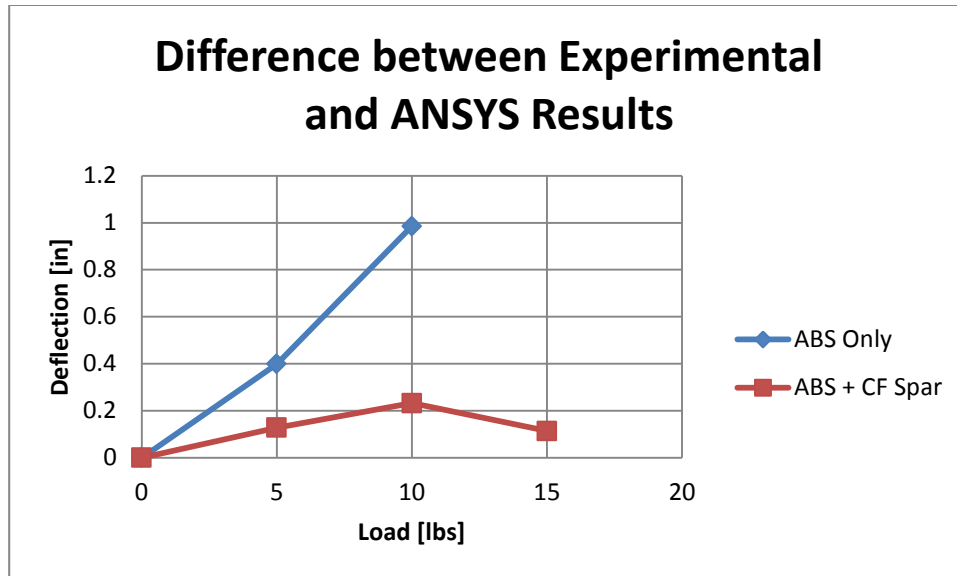


**Figure 36:** Difference between experimental and ANSYS results

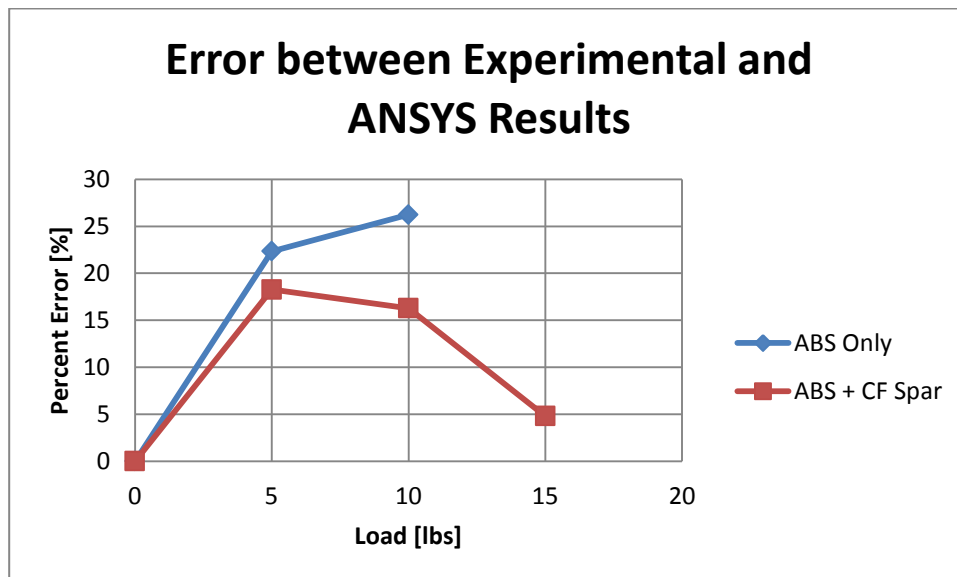


**Figure 37:** Error percentage between experimental and ANSYS results

Results showed that the worst case scenario had a 30% error while the best case, excluding starting point, had a 5% error. Such discrepancies could be due to any of the complications noted above, including complex geometries, material properties, and manufacturing techniques. Given these difficulties and the relatively new use of the material, a 30% error was believed to be acceptable by both the team and the Stratasys coaches. Furthermore, the results of the ANSYS and experimental testing provided sufficient evidence that the aircraft could easily survive typical flight loads with a healthy margin of safety.

## Propulsion Test

A step forward was taken after the propulsion analysis in MotoCalc and a new propulsion wind tunnel test was performed in order to check the accuracy of the system selected. The main goal of this wind tunnel test was to determine the motor thrust, power and efficiency not only at a zero wind state but also at different speeds which simulate a real flight in air. For this new step, two tests were performed:

1. Test 1: Performed at the Armstrong Building Wind Tunnel at Purdue University. This test consisted on a handmade wooden structure in which all the avionics were fitted. The results obtained were closed to the one expected by MotoCalc. However, a second and more reliable test needed to be performed due to partial deflection of the structure during testing.
2. Test 2: Performed at The Boeing Tunnel at Purdue Airport. The wind tunnel foamy airplane was selected as the structure for the motor to be mounted so that it would bring closer results to reality. Results were very similar to those obtained not only by MotoCalc, but also by Professor Sullivan's Excel worksheet.



**Figure 38:** Test 1 at Armstrong wind tunnel (Purdue Univeristy)

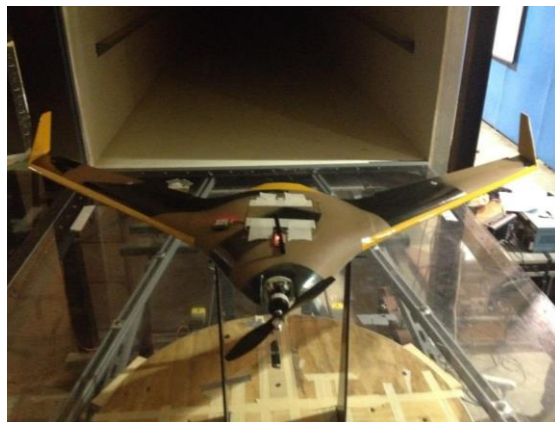


**Figure 39:** Test 2 at the Boeing wind tunnel (Purdue Airport)

Due to the restricted dimensions of the wind tunnels and the fact that the real model was not completed by that time, the team decided to adapt the tests to the dimensions of the foam model (3/4 scale of the 3D printed plane). In order to do so, the following elements were used for the analysis:

- Motor: Parkzone 480.

- 9.5x7.5" propeller.
- 11.1V 2650 mAh batteries.

As mentioned before, the team got the expected results after several iterations at different percentages of throttle power and wind tunnel velocities. Comparison of the results obtained from the three (3) of the sources the team has had access to:

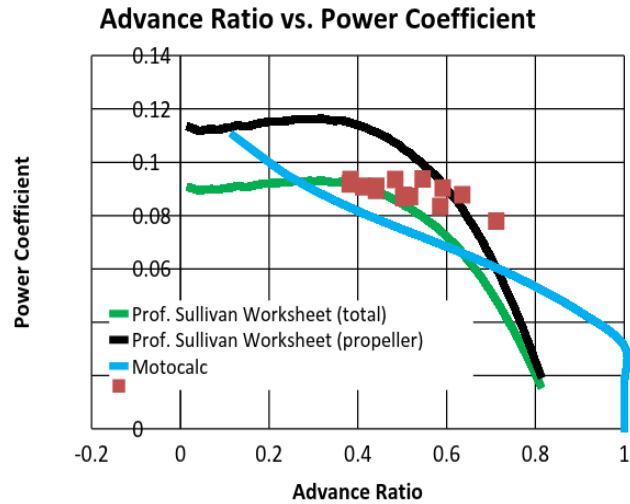


**Figure 40:** Power Coefficient vs. Advance Ratio

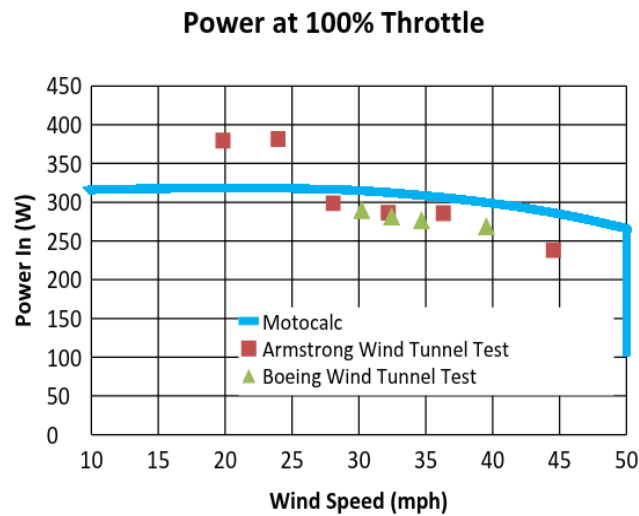


**Figure 41:** Power vs. Wind Speed

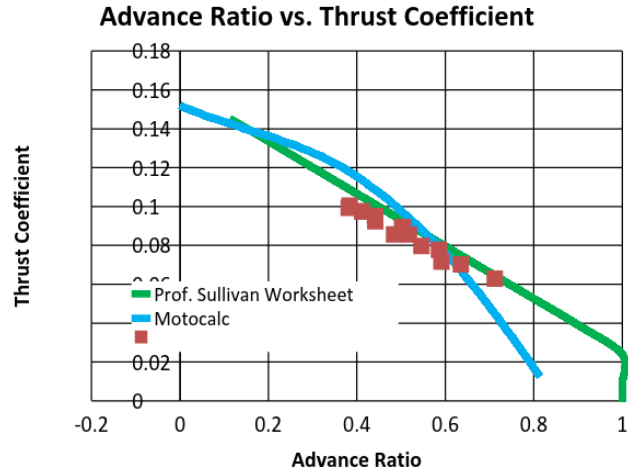


**Figure 42:** Thrust Coefficient vs. Advance Ratio

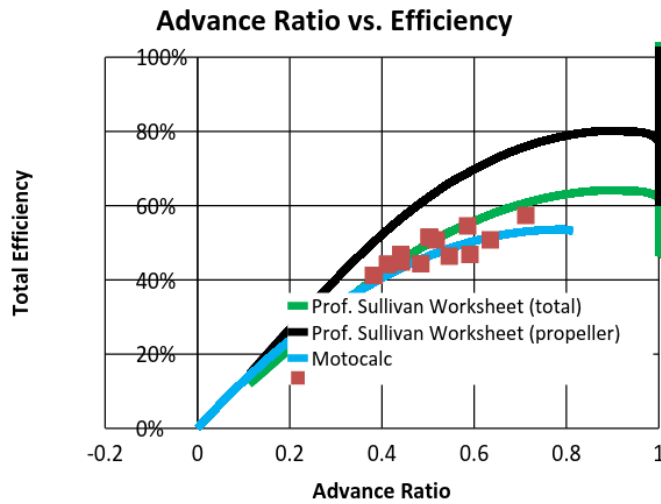


**Figure 43:** Total Efficiency vs. Advance Ratio

Figures 40 through 43 show the accuracy of the work done in previous tests with different systems. As one can easily appreciate, the results obtained from the wind tunnel are very close to the ones calculated from both MotoCalc and Professor Sullivan Worksheet. One of the possible reasons of some discrepancies at the end of some curves might be the loss in power of the battery as the test progressed.

### Structural Testing

Due to the nature of 3D printing process, the bulk material properties of plastic used would not necessarily reflect the strength, weight, or stresses within the finished parts. Furthermore, the methods used to adjust the strength and rigidity of parts designed for additive manufacturing are not the same methods used for solid parts that are to be machined to shape. For example, to increase the strength of a wing section, the increasing the internal rib density would have a much greater effect than increasing the rib thickness. On the other hand, increasing the skin thickness of the printed wing would increase rigidity and weight of the wing more than increasing the rib thickness.

The orientation of the part during the printing process, for example, would alter the strength in various directions. The complexity of the shape of the parts, in addition to the complexity of performing analyses on anisotropic materials, drove the team to decide that physical testing of full scale printed parts would be valuable for determining the structural properties of the proposed design. The team also consulted with Stratasys many times before determining how the parts were to be designed and printed before testing.



**Figure 44:** Woven (top) and pultruded (bottom) carbon fiber tubes used in testing

It was decided that a 3d printed body, reinforced internally with carbon fiber tubes, would be used for the fuselage and the wings of the final UAV. The design was to transfer torsional loads outward to the wingskin, and bending loads inward to the carbon fiber tubes as well as outward to the wingskin. The carbon fiber tubes were tested alone initially.

Three lengths of pultruded  $\frac{1}{2}$ " carbon fiber spar were tested in a three point bend test. The tubes failed in crushing rather than bending, regardless of the fixtures used. This raised concerns about the type of CF tube used. A woven tube would have fibers in the transverse direction, and therefore would be more resistant to crushing, so woven tubes were tested in the next testing phase.

The next testing phase tested the 3D printed material, and the CF tube spar selection. Two test pieces were printed, which were wing sections with added supports for ease in testing. Several tests were carried out on the two test pieces, with and without the CF tubes.

The simple bending test used two spars, pultruded and woven CF spars, and two wing pieces, one with a single printed layer skin thickness, and another with two layers of printed material for the skin.



**Figure 45:** Wing testing apparatus with carbon fiber spar



The woven CF tube outer diameter was too large to fit inside the wings, so it was sanded down to size in a lathe. The carbon fiber tube was inserted into the wing, which was bolted onto the testing plate. To facilitate quick swapping of the spars, an access hole was drilled into the plate. The plate was then clamped into a vice on a milling table, to provide a flat, rigid surface from which height measurements could be taken.



**Figure 46:** Wing testing apparatus

Loading was done by hand, slowly, to prevent plastic deformation of the test pieces. A spring force gauge was used to measure the load, and a height gauge was used to measure tip deflection. To verify that no plastic deformation took place during loading, the height was checked after load was released. In every case, the wing came back to the original position.

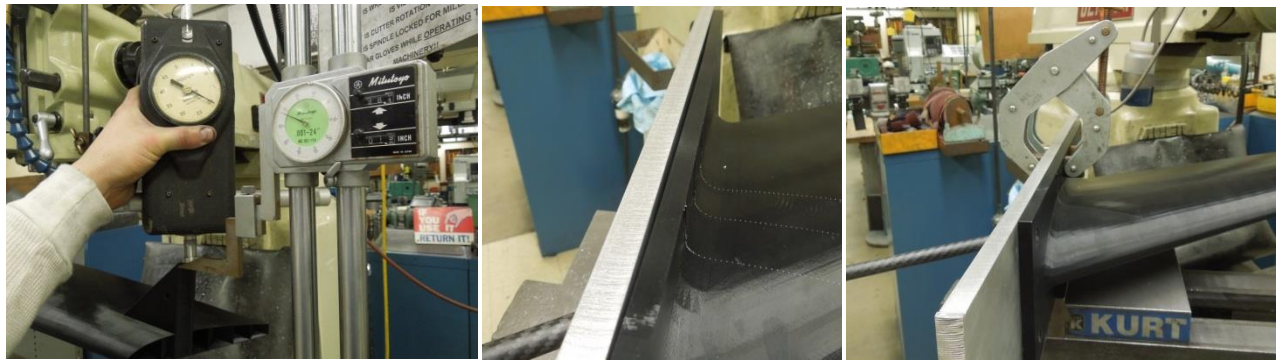


**Figure 47:** Wing testing process

Initially, the wing was bolted to the test plate. Immediately after the first downward load was applied, the wing began to flex and separate from the top of the plate. To prevent this separation, the wing was clamped to the plate on the top edge. The wing did not separate with the clamps in place.

The plate was not moved between testing the two different wing specimens. One was unbolted, and the other was bolted in its place. The same initial position (for zero deflection) was able to be used for both specimens. Bending test results are within the table below:



**Table 3: Wing bending test results**

<b>Wing Ply</b>	<b>Spar Inserted</b>	<b>Bending Load (lbs)</b>	<b>Deflection (inch)</b>
Double	Woven	5	0.440
Double	Woven	10	0.822
Double	Woven	15	1.622
Double	Woven	20	1.932
Double	Pultruded	5	0.440
Double	Pultruded	10	0.795
Double	Pultruded	15	1.294
Double	Pultruded	20	1.744
Double	None	5	0.466
Double	None	10	1.034
Double	None	15	1.865
Single	Woven	5	0.705
Single	Woven	10	1.435
Single	Woven	15	2.435
Single	Pultruded	5	0.700
Single	Pultruded	10	1.424
Single	Pultruded	15	2.370
Single	None	5	1.784
Single	None	10	3.756

The weight of each test piece was recorded as well:

**Table 4: Component weights**

<b>Component</b>	<b>Weight</b>
1 ply wing	552 g
2 ply wing	691 g
Woven spar	80.7 g
Turned woven spar	70.3 g
Pultruded spar*	48.2 g
*The pultruded spar is about 4 inches shorter than the 36 inch woven spars.	

The bending test showed that the pultruded spar had better performance, and weighed less than the woven spar. The inclusion of a spar had a large effect on bending deflection under load, so the design did transfer the loads into the tubes, as desired. The difference between the single ply wing skin and double ply wing skin in weight and strength were recorded.

The next test was the torsional test. The wing piece was bolted to the test plate. The clamps were placed just as with the bending tests. The wing did not separate with the clamps in place. When in torsion, the carbon fiber spar did not affect results, because the spar was round, fit without gluing, and ran along the axis of rotation.

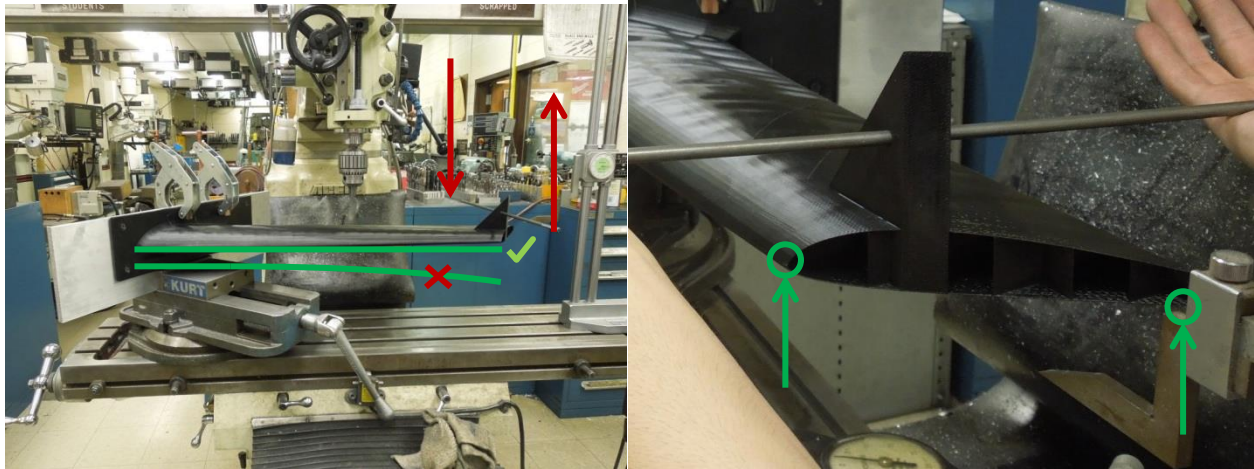


**Figure 48: Wing torsion test**

The tip of the wing test pieces had triangular testing tabs, which had through holes added for the purpose of the torsional tests. The testing tab had a through hole that had to be reamed to  $\frac{1}{4}$ " diameter to accommodate the testing rod. The testing rod was 18" long, and was centered on the testing tab. The force gauge was used to measure the perpendicular load on one side of the rod, and then the height gauge was used to measure the bending. The opposite end of the rod was then loaded upward, and the bending measured.

Once the bending was verified to be zero, then the two forces were equal, and therefore a pure torque was being applied on the wing. With the pure torque applied, the height gauge was used to measure the vertical position at two places on the wing.

From these points, a maximum change in angle could be calculated. The results are recorded in the following table:

**Table 5: Wing torsion test results**

Wing Ply	Load (lbs)	Torque (ft-lbs)	Point one (inch)	Point two (inch)	$\Delta\theta$ (decimal degrees)
Single	10	7.5	3	4.602	3.72
Single	20	15*	3	4.42	6.93
Double	10	7.5	4	4.178	1.16
Double	20	15	4	4.29	3.96
Double	30	22.5*	4	4.503	5.41
*The testing rod began to deform the testing tab at this load, although the wing was still intact. How much of the twisting in the wing was reduced by the tab deformation is not immediately apparent.					

After measurements were taken, the loads were removed, and the wing was measured again to verify all displacement was elastic.

The wing was unchanged, but the hole in the testing tab was compromised, as evidenced by the testing rod being able to move without the testing tab moving, as illustrated by the colored lines in the photo.



**Figure 49: Wing torsion test**

### **Payload Testing**

There were two parts to the payload testing. The first part was the testing of the Tetracam NDVI camera, which was accomplished by taking several images outdoors of various living and non-living objects. It is required that the first picture taken be of a calibration card to gauge the spectrum of light that day, which then calibrates the subsequent images. After the images were taken, they were downloaded and processed into Tetracam's proprietary software for processing. The image of the calibration card defines the parameters for converting the images into NDVI, and then all of the subsequent images are processed in a batch operation converting them to NDVI images and indexes. Finally, after the images were processed, they were loaded into an image stitching program, Kolor's Autopano Pro. Using default settings, the images were successfully stitched.

The second part of testing was wiring the camera power and signal with the video transmitter, and testing the functionality. Once powered on, the transmitter connected to a receiver in the ground station and displayed the video to a small TV. The system worked well, and the transmitter did not get excessively hot.

### **Autopilot Test**

It was decided that an autopilot system was necessary because it allows an entire field of crops to be imaged in a short period of time. The system will allow the aircraft to fly straight and level and make turns at specified locations and altitudes. Ardupilot was chosen for the autopilot system because it is cost effective and user friendly. The autopilot system was initially tested using a flight simulator. The Ardupilot system was connected to the X-Plane flight simulator to insure the software could fly a virtual plane on the mission waypoints. After successfully demonstrating the autopilot in the flight simulator the hardware was installed on the foam scale model for initial flight testing.

The goal of the first flight test was to command the plane to fly in "stabilization mode" which means the airplane will fly straight and level. Initially the plane stabilized in the yaw and roll orientations but pitched nose down causing the vehicle to descend rapidly. Several further tests were performed by

systematically adjusting the pitch gains and retesting “stabilize mode”. The aircraft endured several minor crashes and motor mount repairs over several days of testing before effective pitch gains were obtained. After effective pitch gains were obtained the aircraft successfully flew straight and level without human input into the controls. Immediately after the aircraft demonstrated the ability to fly in “stabilize mode” the aircraft was commanded to follow several predetermined waypoints. The aircraft successfully followed the waypoints. Figure 50 below shows the aircraft flying in circles around the launch area without any human control input. The aircraft was flying in 12 mph winds which caused the circles to stretch into ovals.



**Figure 50:** Successful demonstration of the autopilot circling the launch site.

Figure 51 shows the autopilot successfully following 2 waypoints while being flown at the Georgia Tech flying field.

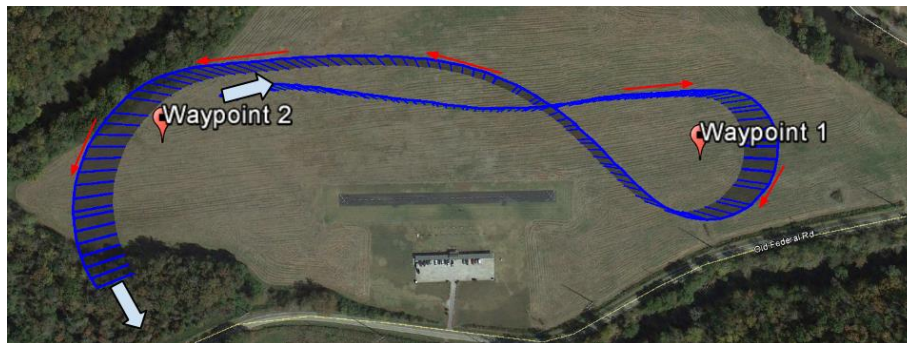


**Figure 51:** Successful demonstration of the autopilot following waypoints.

## Flight Test

This section covers all the work done from the very beginning of the course. It is important to remember that the Team 3 final design comes from long periods of brainstorming and has passed to different stages during the past months. That is the reason why ‘flight test’ does not only refer to the final design, but also to the two previous prototypes which have performed their objectives as expected:

1. Foamy model 1.0. This was the first concept that Team 3D came with and was intended to perform some rudimentary aerodynamic tests. This first prototype consisted of two wings together with two thicker fuselage sections (split horizontally down the chord line). It was constructed entirely on a foam cutter for simplicity. In addition to mounting in a wind tunnel, a gliding testing was also performed in which the stability of the plane could be examined. Figure 52 shows it gliding successfully.





**Figure 52:** Ignacio hand launching the first foam glide model

2. Foamy model 2.0. The second prototype proved to be the most useful, as it exactly replicated the shape of the final design on a  $\frac{3}{4}$  scale. It was used for wind tunnel testing, flying demonstrations, pilot orientation, and autopilot testing. Designed to fit all the avionics as well as the motor mount and batteries, this plane became not only the preceding step to the final concept, but also one the main sources of information thanks to numerous real flights. All three different launching methods could be successfully performed with this 2.0 model.
  - a. Hand launching: this was initially the only way of launching the aircraft until new ideas were approved. Most of the attempts were satisfactorily completed. Apart from security, the only concern that the team could appreciate about this launching method was the way in which the person in charge throws the plane since it could cause the loss of control of the aircraft. However, it was also shown that this method does not require any special experience and any non-skilled operator could perfectly hand-launch it.
  - b. Catapult launching: satisfactory tested the day of the presentation. However, the team is concerned about the need of increasing the power and speed in order to be sufficient for the real 3D printed model. No more tests have been performed due to the location of each element during the course since plane and launcher were both made in different schools.



**Figure 53:** Scott firing the scale model from the catapult launcher

- c. Cart launching: satisfactory tested in different situations, including a smooth runway the day of the presentation in Atlanta and a bumpy one at one of the Purdue farms. Figure X shows the aircraft lifting up from the cart despite crosswind perturbations.



**Figure 54:** Scale model takes off from launch cart

Not only have launching methods been tested, but also the ArduPilot and landing method. The aircraft succeeded in following predetermined waypoints in automatic mode and was able to stabilize itself during its trajectory. Landing on the skids was always achieved although the team is concerned about the possibility of breaking a non-folding propeller and will keep on looking for different ways to solve this issue.

3. Final fully 3D printed model: although it has not flown yet, the aircraft is already set to take off, perform the mission and land. Team 3D is expecting to be able to fly within the next weeks with the cooperation of weather.



**Figure 55:** Team 3D standing behind the completed aircraft and launcher

## Manufacturing & Assembly

### Methodology

Fused Deposition Modeling (FDM), a specific 3D printing technique, was the chosen method for manufacturing the main structural components of the aircraft (i.e., fuselage, wing, winglet, elevon, elbow joint, and payload module). Additional carbon fiber tubes, wooden brackets, and an aluminum joint was used to structurally reinforce, attach the motor, and join the two halves of the body. Please refer to manufacturing drawings in [Appendix\(CAD Drawings\)](#) for part manufacturing descriptions and locations. The FDM process is an additive manufacturing method where a cross section of the structural part is printed layer by layer, incrementally. FDM has become much more popular in the UAV industry as the technology has developed and become more available to the public. The advantages of 3D printing include the following: replaceable parts, low manual labor costs, relatively inexpensive material costs, and minimal time needed to assemble.

Minimizing the use of support material is the main objective in order to obtain low build time costs. Recently, the engineers at the University of Sheffield's Advanced Manufacturing Research Center (AMRC), as a joint effort with Boeing, released the design of a blended-wing UAV. This design entailed two fully self-supported parts that could be printed within 24 hours (FDM-Printed fixed wing UAV, 2014).



**Figure 56:** AMRC Aviation fully self-supported FDM blended wing body (Wingspan: 1.5m)

A Stratasys Fortus 900 printer has the capability of manufacturing a part with a base of 3x3 feet and a height of 2 feet. It also has the capability of printing a structure that is one filament thick (e.g., 0.016 inches, 0.020 inches). With this new printing technology, the amount of excess material can be reduced substantially and the limits of optimization of a part are essentially limited only by the geometry of the print (i.e., a fully self-supported print can only range between 0 to 45 degrees from the vertical axis without needing support material).

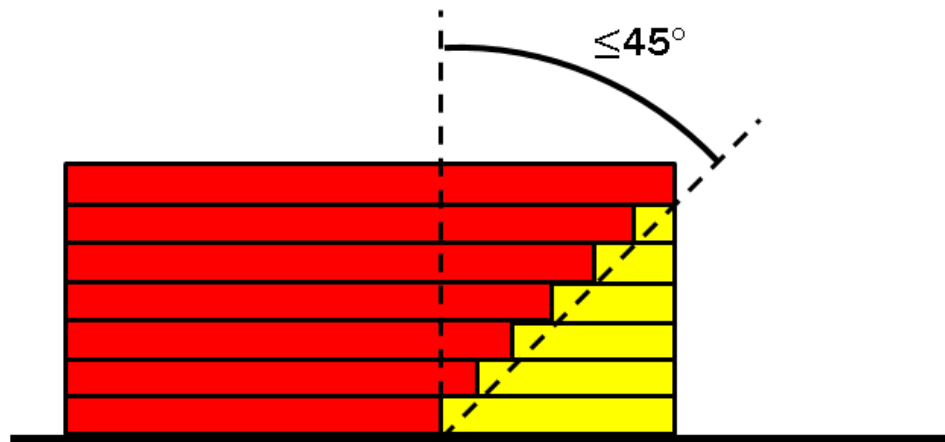


**Figure 57:** Design constraint for printing a fully self-supported structure

The FDM process is fully automated once the part has correctly been modeled using a Computer Aided Drafting (CAD) program. Because the CAD involved in designing the printed parts is extensive and intricate, CATIA V5-R2012 was used for its surface modeling capabilities. The advantage of having a fully automated manufacturing process limits the possibilities of human error in manufacturing and decreases the amount of manual labor involved in the process. This accumulates to a substantial decrease in labor costs eventually.

### Collaboration

Due to the chosen manufacturing method, assembly of the aircraft was fairly quick and simple and so there little inter-university collaboration was needed on the manufacturing and assembly of the vehicle. The team had decided that after the parts were printed by Stratasys, they would be sent to Purdue for final assembly and integration with the payload module. The final launching method, a catapult system, was being built between teams at Georgia Tech, and would be employed by our team as well. There was much more in-depth CAD work required in order to 3D print the aircraft when compared with more traditional methods of aircraft manufacturing. As such, the CAD work completed at Brigham Young University was considered to be a part of the manufacturing process.

### Tooling & Jigs

Due to the unique 3D printing manufacturing technique chosen, very little tooling was required to assemble the aircraft. In cases where screw or pin holes were required, locator holes were included in the 3D printed part and were simply drilled out with an electric hand drill at the time of assembly. Ribs and shelves for the payload module were machined using the router at the Purdue University machine shop. The aluminum joining plate in the aft portion of the body was milled out of aluminum using a CNC mill. Other tooling required included screwdrivers, allen keys, and a Dremel tool. The only jig used in the assembly of the aircraft was a foam jig used to locate and glue the pieces of the payload module together. This jig is shown with the payload module in Figure 58.



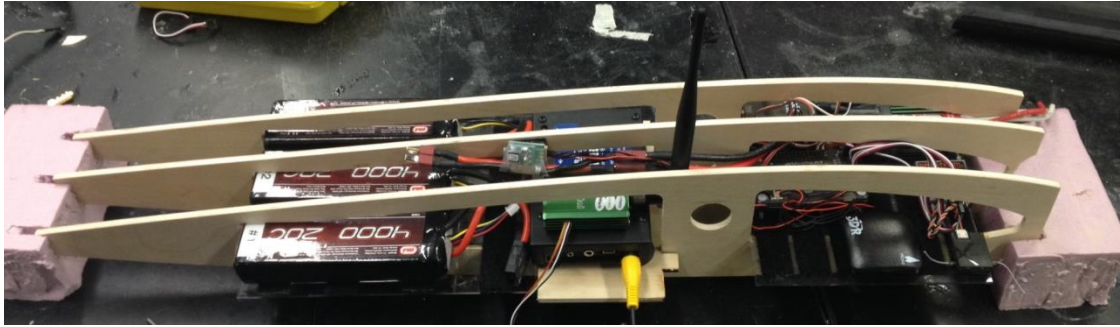


**Figure 58:** Payload assembly jig

## Assembly

Final assembly of the aircraft was done at Purdue University following the assembly drawing shown in Figure X. The first step was to mount the servos and feed the wires through to the payload module. Next, landing skids were slid into their printed slots. The elbow joint was then glued in place on each side of the body. The wing spars were slid in place and the wings were attached by sliding them onto the spars and adding a pin along the trailing edge to take torsional loads. The winglet was attached with two pins and epoxied in place. Five pin hinges were epoxied in place along the trailing edge of each wing and the elevons were then attached to the wing. Set screws were used to fix the pin hinges onto the elevons, allowing them to be removed for disassembly of the aircraft.

The payload module was assembled separately using epoxy to fix the pieces together as shown in Figure 59. Once the two halves of the aircraft were assembled, the payload module was slid into place, the body spar was fixed into the elbow joint, the motor was mounted to the forward bulkhead, and the aluminum joining plate was slid into the slot aft of the payload bay. The two halves of the aircraft were then joined together and assembly was complete.

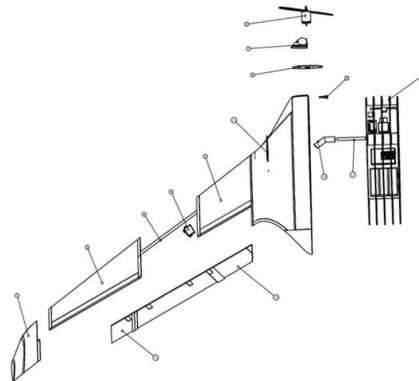


**Figure 59:** Assembly drawing of final design

## Additive Manufacturing

In designing for the FDM process, a medium between structurally sound geometry, weight, and skin thickness was obtained. From the structural analysis, a one layer thick skin was determined to be sufficient for the structural theoretical loads. Theoretically, the 0.016 inch thick ribs were supposed to be able to transfer the pressure loads throughout the entire skin evenly. Hence, the ability to print a structurally sound part that was one layer thick throughout.

The process of CAD modeling for FDM was extensive because of the surface and solid interfaces. Each surface within the CAD model represented the center of the extruded filament (where the skin and rib filaments were 0.016 inches and 0.020 inches thick). These surfaces were all derivatives of the Outer Mold Line (OML) of the blended-wing body. The following images are of each part in their printed orientations.

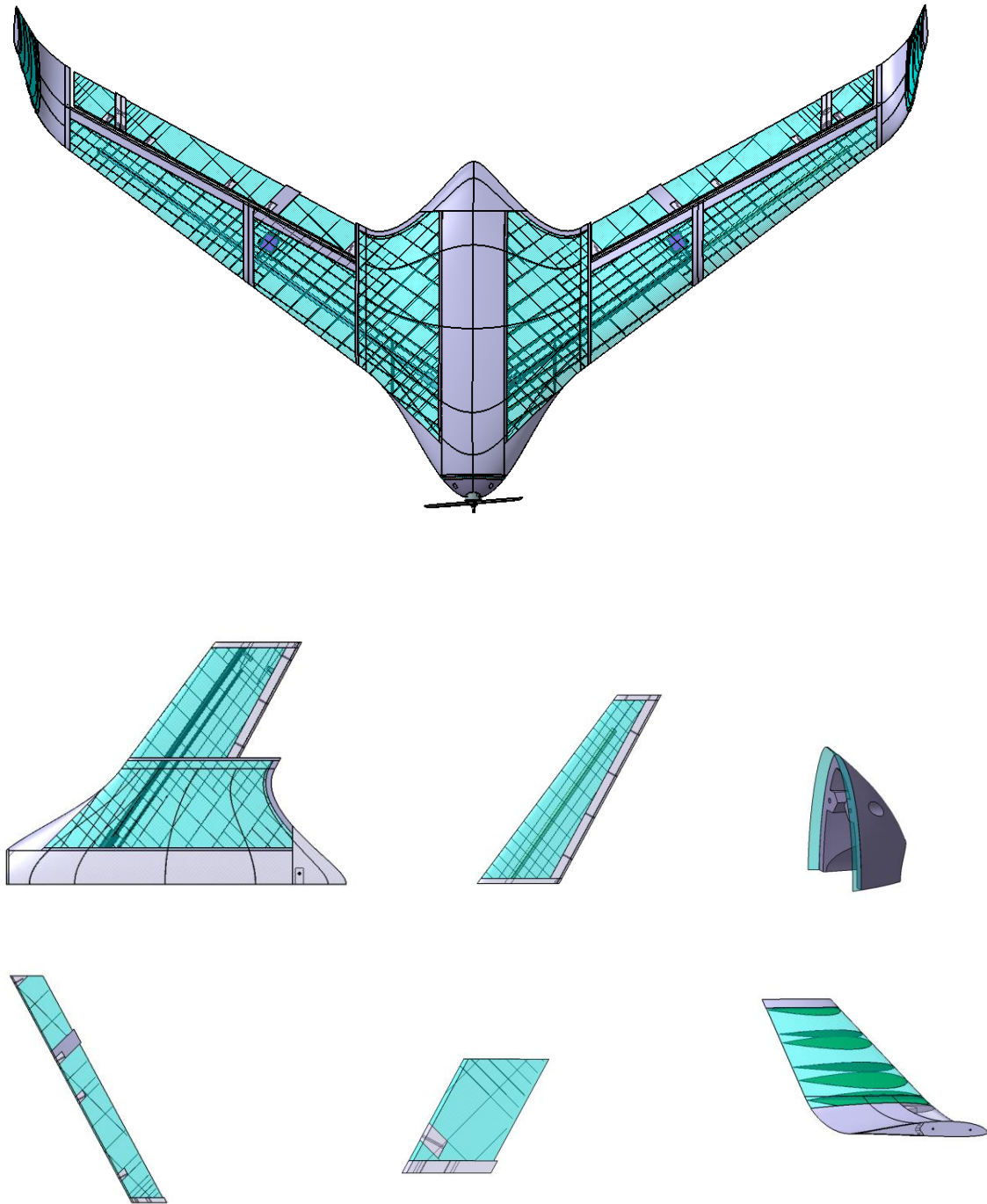


**Figure 60:** Self-supported FDM prints in their respective printing orientation

For specific regions that needed more support, these regions were modeled as solid parts and were assigned specific honeycomb densities via Stratasys processors (e.g., drill holes and etc.). Please refer to [Appendix \(CAD Drawings\)](#) for solid and surface modeling design methods.

## Bill of Materials

A Bill of Materials was compiled to keep track of all materials and components required to assemble the aircraft. The Bill of Materials is shown in Table 6 and is organized by functional group.

**Table 6:** Bill of Materials

Section	Component	Qty	Details
<b>Structures</b>	L Body	1	3D Printed Part
	R Body	1	3D Printed Part
	L Wing	1	3D Printed Part
	R Wing	1	3D Printed Part
	L Winglet	1	3D Printed Part
	R Winglet	1	3D Printed Part
	L Elevon	1	3D Printed Part
	R Elevon	1	3D Printed Part
	Motor Cover	1	3D Printed Part
<b>Integration</b>	Wing CF Spar	2	0.5" x 32.5" pultruded CF tube spar
	Body CF Spar	2	0.5" x 6" wrapped CF tube spar
	Elevon hinge	10	Point hinge
	Joining plate	1	Aluminum rectangular block
	Joining screws	2	Machine screws & washers
	Elevon set screws	10	Small wood screws
	Torsion pins	6	1/8" x 1" aluminum rod
	NDVI imager	1	Tetracam ADC Lite
	Camera battery	1	Zippy 2200 mAh 3S1 25C
<b>Payload</b>	Video transmitter	1	ReadyMadeRC 400mW 1300MHz
	Payload Module	1	Plywood & acrylic shelf unit
	Motor	1	AXI 4130/16 electric motor
	Motor Mount	1	Cross mount
	Mounting Screws	4	Screws & washers supplied with motor
	Mounting Nuts	4	Locking nuts
	Propeller	1	16x8" composite propeller
	Battery	1	Zippy 5000mAh 6S 45C
	Speed Controller	1	Castle phoenix edge lite HV 60
<b>Avionics</b>	Battery Eliminator	1	Castle CC BEC 6S
	Autopilot	1	APM 2.5 Ardupilot
	F-F Cables	10	12 cm avionics wiring cables
	M-F Cables	10	30 cm servo cables
	Receiver	1	Spektrum AR8000 8-channel
	Elevon Servo	2	Hitec HS-465 MG
	GPS & Compass	1	3DR uBlox GPS w/ compass kit
	Radio set	1	3DR radio 915 MHz

## Repairability

One of the main hopes behind a 3D printed airframe was that repairs are quick and easy, because new parts can be printed in short time periods and for little cost. Unfortunately, the reparability of the 3D printed airplane is very poor. After an incident during an initial flight test, the forward bulkhead where the motor mounts was shattered and unusable. Unfortunately, the design of the core pieces around the payload module were such that the forward bulkhead was not separable from the rest of the payload module shroud. As evidenced by the repair attempts before the flight test at Georgia Tech, repairs are difficult, and employ classical construction techniques such as wood, epoxy, and fiberglass.

For other sections of the vehicle that are not structural members and composed of honeycomb-style solids, epoxy worked well for sealing the plastic and reinforcing areas where the very thin skin had been punctured.

## Cost Update

An outline of the project spending by functional group is shown in Table X. The total cost of the aircraft was approximately \$7,000. The cost was approximately \$1,000 higher than initial estimations but the project still came in under the allotted budget of \$10,000. Remaining funds were used for prototyping, testing, and travel to the flight demonstration at Georgia Tech at the end of the semester.

**Table 7: Cost Update**

Component	Cost
Payload	\$4,500.00
Propulsion	\$350.00
Avionics	\$750.00
Battery	\$130.00
Structure	\$300.00
Servos	\$170.00
Launch	\$800.00
<b>Total</b>	<b>\$7,000.00</b>

## Lessons Learned

The team faced many challenges throughout the design process in the AerosPACE course and has learned some valuable lessons from those challenges. First, we learned that a face-to-face kickoff meeting at the beginning of the design process would have been very helpful. It is easier to work with someone when you know them as a person instead of just an email address. Second, individual responsibilities should have been defined earlier in the design process. This would have allowed each individual to become more of an expert in the area in which he or she is focused. Third, it was found that accountability improves productivity. Halfway through the design process, the team leader started requiring each team member to present at each team meeting to show their progress over the past week. Individual team members were much more likely to make progress each week when they were held accountable in this way. Fourth, using meeting agendas proved to make each team meeting much more effective. Fifth, it was found that it would be helpful if the lectures and labs associated with the AerosPACE course were scheduled so that all team members can attend. Finally, the team believes that some private team meetings might have led to better cohesion among team members. People tend to act very professionally when outside observers from The Boeing Company are present in team meetings, making it difficult for

team members to get to know each other as friends. This is important because it is much easier to work with someone to whom you can relate.

Besides the lessons learned pertaining to teaming, some discoveries were made regarding collaboration tools. First, the team preferred to use Webex for team meetings. Webex has an excellent screen sharing tool and also allows users to join by phone when no internet connection is available. Also, this system is accessible from within The Boeing Company for those Boeing employees joining us during meetings. Despite these advantages, the team switched to Google Hangouts for team meetings due to scheduling conflicts within Webex. The team chose Google Hangouts because it is free and easy to use. Second, the team found that Google Drive was most effective for file sharing between team members. Third, the team believes that CorpU could be improved by implementing a file organization and searching system like that present in Google Drive.

## **Conclusion**

As a multi-university collaborative project, not only was a blended wing UAV successfully designed using standard aeronautical design tools, but the boundaries of the UAV industry was also expanded by creating a 7.5' wingspan, fully-self supported, and additive manufactured (AM) UAV structure. Although AM is a relatively recent application in the UAV industry, integrating the standards used in aeronautical design and utilizing this new technological manufacturing method will continue to push the boundaries of UAV design. In the future, the structural analysis of these AM parts will continue to be investigated and developed in order to more accurately perform numerical structural analysis. New developments in the structural analysis (FEA) of AM parts will further the optimization capabilities in AM UAV design and will eventually provide cheaper and more available UAV's to the public.

## **References**

*FDM-Printed fixed wing UAV*. (2014, 3 14). Retrieved 4 20, 2014, from amrc.co.uk:  
<http://www.amrc.co.uk/featuredstudy/printed-uav/>

RCGroups. (2013, Jan 14). *Skywalker X8 catapult*. Retrieved from:  
<http://www.rcgroups.com/forums/showthread.php?t=1806237>

## **Appendix A: CAD Drawings**

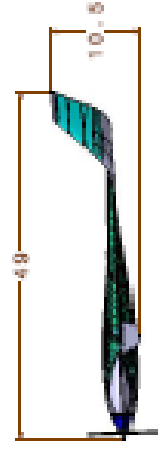
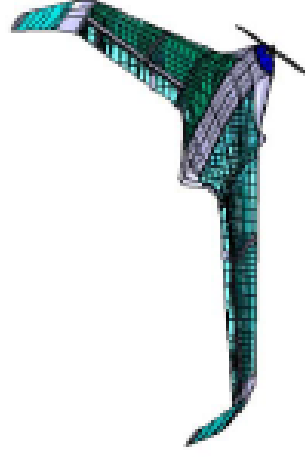
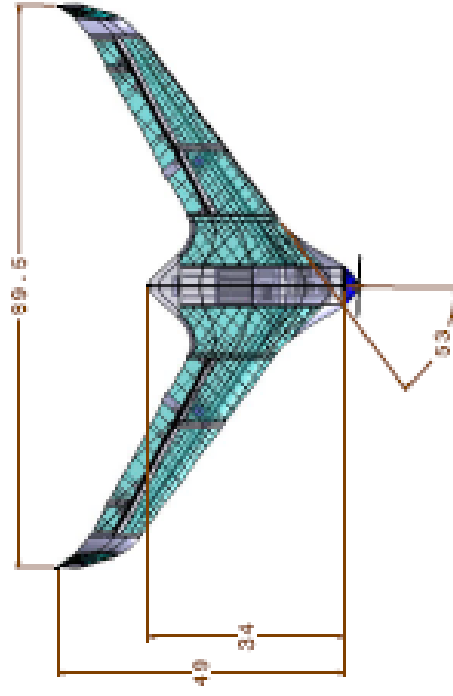
### List of Drawings

1. Overview 3D
2. Overview
3. Payload Arrangement
4. Left Fuselage
5. Left Fuselage Structural Arrangement
6. Left Wing
7. Left Wing Structural Arrangement

Overall Dimensions:

Planform Area: 8 ft<sup>2</sup>

Wingspan: 89.5"

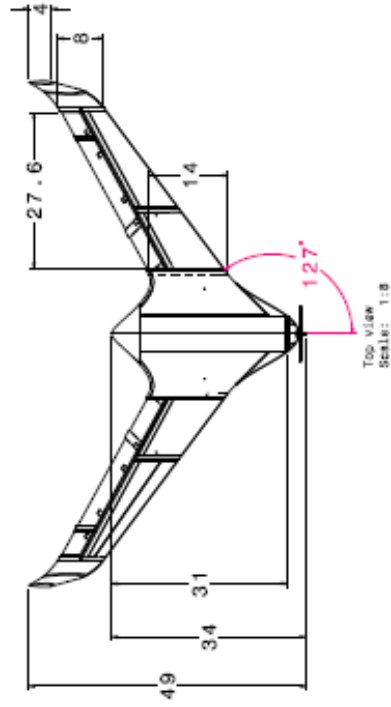


Note: All dimensions are in inches unless otherwise noted

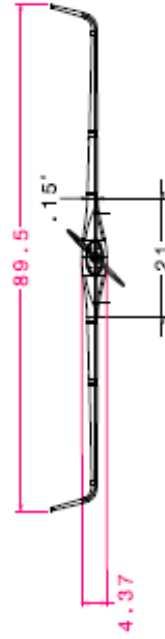
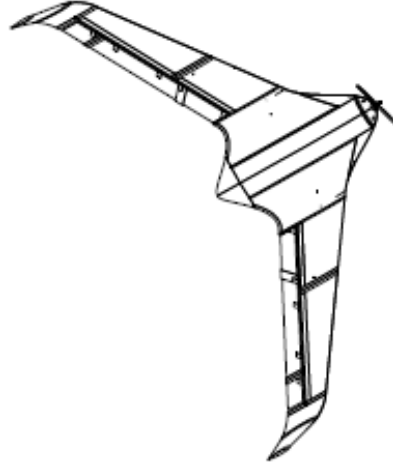
Title: 3D		Date: 10/1/2023	
Author: 10/1/2023		Revision: 1.0	
Drawn: 10/1/2023		Scale: 1:1	
Sheet: 1 of 1		Total: 1 of 1	



Overall Dimensions:  
 Planform Area: 8 ft<sup>2</sup>  
 Wingspan: 89.5"



Isometric view  
 Scale: 1:8

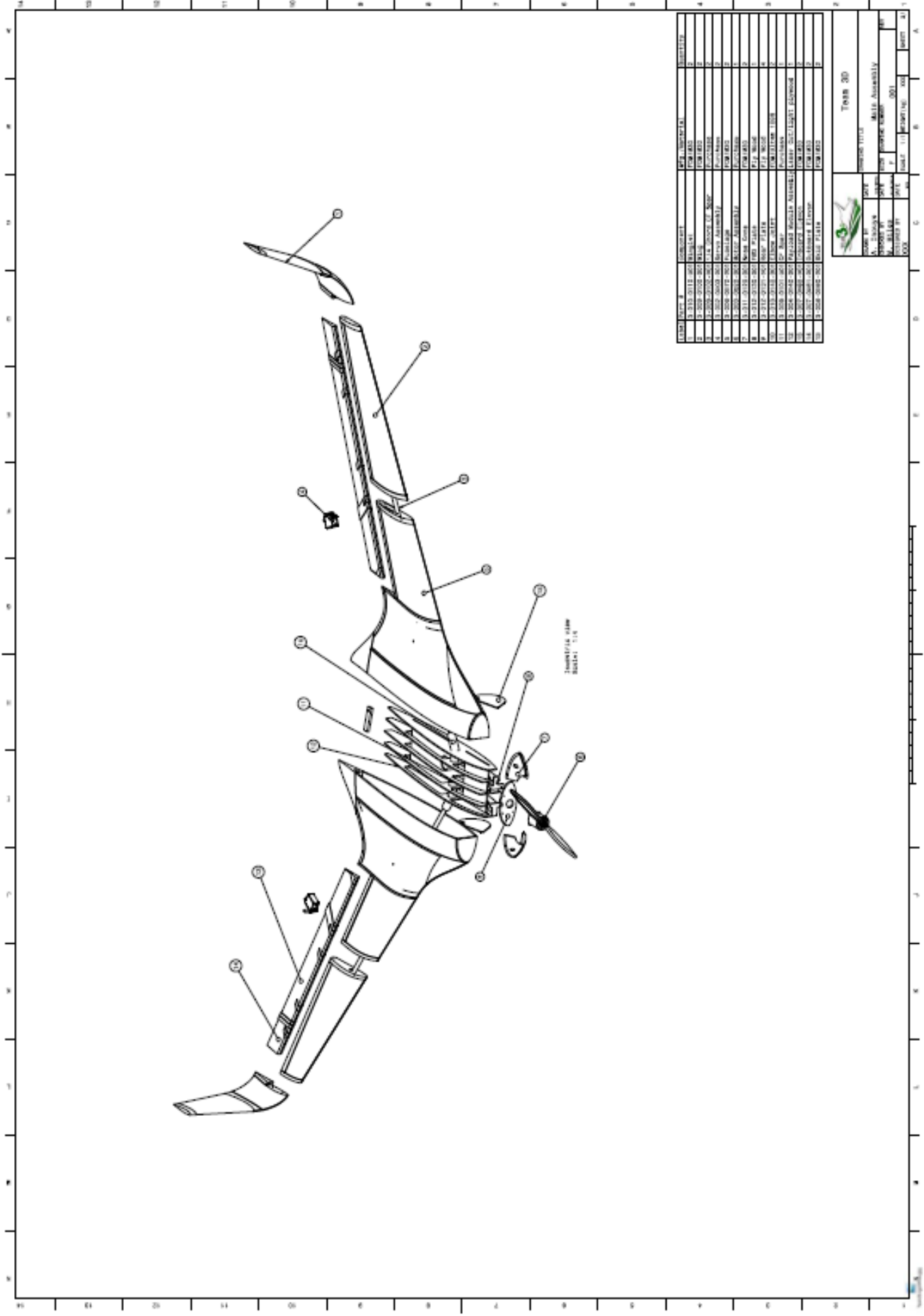


Right view  
 Scale: 1:8



Team 3D		Team 3D	
Team 3D	Team 3D	Team 3D	Team 3D
A. HARRIS	A. HARRIS	A. HARRIS	A. HARRIS
B. HARRIS	B. HARRIS	B. HARRIS	B. HARRIS
C. HARRIS	C. HARRIS	C. HARRIS	C. HARRIS
D. HARRIS	D. HARRIS	D. HARRIS	D. HARRIS
E. HARRIS	E. HARRIS	E. HARRIS	E. HARRIS
F. HARRIS	F. HARRIS	F. HARRIS	F. HARRIS
G. HARRIS	G. HARRIS	G. HARRIS	G. HARRIS
H. HARRIS	H. HARRIS	H. HARRIS	H. HARRIS
I. HARRIS	I. HARRIS	I. HARRIS	I. HARRIS
J. HARRIS	J. HARRIS	J. HARRIS	J. HARRIS
K. HARRIS	K. HARRIS	K. HARRIS	K. HARRIS
L. HARRIS	L. HARRIS	L. HARRIS	L. HARRIS
M. HARRIS	M. HARRIS	M. HARRIS	M. HARRIS
N. HARRIS	N. HARRIS	N. HARRIS	N. HARRIS
O. HARRIS	O. HARRIS	O. HARRIS	O. HARRIS
P. HARRIS	P. HARRIS	P. HARRIS	P. HARRIS
Q. HARRIS	Q. HARRIS	Q. HARRIS	Q. HARRIS
R. HARRIS	R. HARRIS	R. HARRIS	R. HARRIS
S. HARRIS	S. HARRIS	S. HARRIS	S. HARRIS
T. HARRIS	T. HARRIS	T. HARRIS	T. HARRIS
U. HARRIS	U. HARRIS	U. HARRIS	U. HARRIS
V. HARRIS	V. HARRIS	V. HARRIS	V. HARRIS
W. HARRIS	W. HARRIS	W. HARRIS	W. HARRIS
X. HARRIS	X. HARRIS	X. HARRIS	X. HARRIS
Y. HARRIS	Y. HARRIS	Y. HARRIS	Y. HARRIS
Z. HARRIS	Z. HARRIS	Z. HARRIS	Z. HARRIS

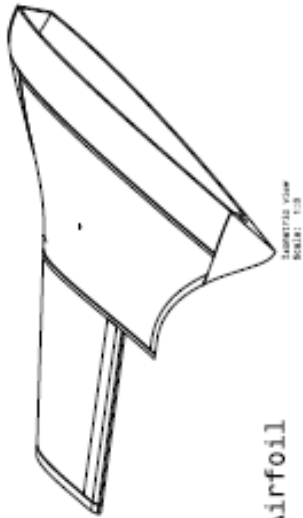
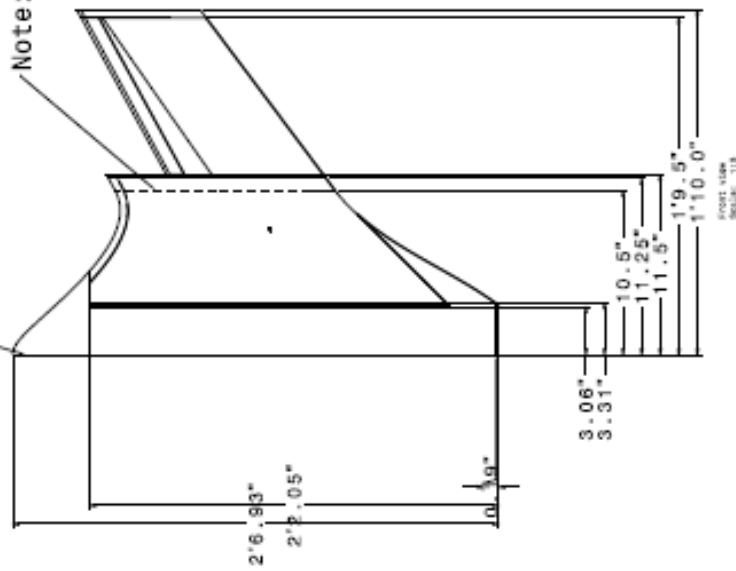
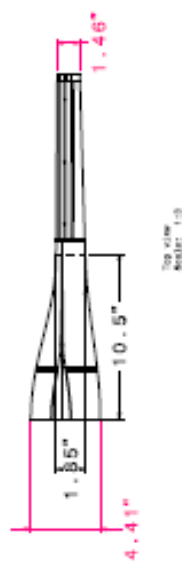
Note: All dimensions are in inches unless otherwise noted



ITEM	QTY	REV	DATE	BY	APP	DESCRIPTION
1	1	1	01/01/2011	001	001	001
2	1	1	01/01/2011	001	001	001
3	1	1	01/01/2011	001	001	001
4	1	1	01/01/2011	001	001	001
5	1	1	01/01/2011	001	001	001
6	1	1	01/01/2011	001	001	001
7	1	1	01/01/2011	001	001	001
8	1	1	01/01/2011	001	001	001
9	1	1	01/01/2011	001	001	001
10	1	1	01/01/2011	001	001	001
11	1	1	01/01/2011	001	001	001
12	1	1	01/01/2011	001	001	001
13	1	1	01/01/2011	001	001	001
14	1	1	01/01/2011	001	001	001
15	1	1	01/01/2011	001	001	001
16	1	1	01/01/2011	001	001	001
17	1	1	01/01/2011	001	001	001

		<b>ITEM TITLE</b> 001	
<b>DATE</b> 01/01/2011	<b>BY</b> 001	<b>APP</b> 001	<b>DESCRIPTION</b> 001
<b>REV</b> 001	<b>DATE</b> 01/01/2011	<b>BY</b> 001	<b>APP</b> 001





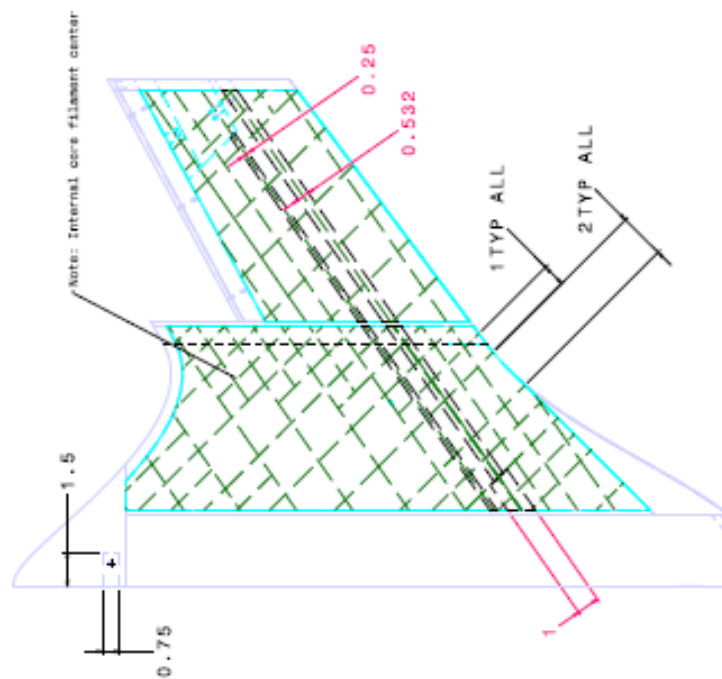
Note: MH 90/NACA 0012 Center Line Chord Airfoil

Note: MH 82 Root Chord Airfoil

\*Note: Reference Left Fuselage.DAT for dimensions

Notes:  
1) ALL PIN AND PIN HINGE JOINTS ARE 1/8" DIAMETER

	NAME OF	DATE	TOTAL (1)	RECEIVING	COST	SALES TAX
	A. BANCAY	2011				
	ISSUED BY	DATE				
	M. BILLO	2011				
	ISSUED BY	DATE				
	ISSUED BY	DATE				
TOTAL						
TOTAL						

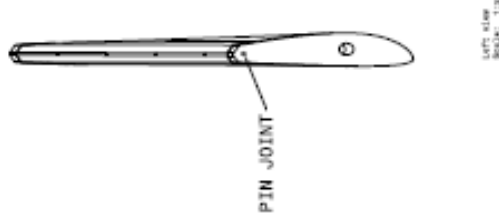
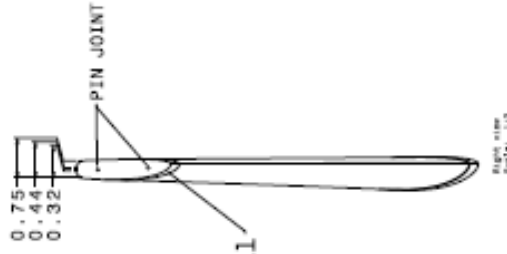
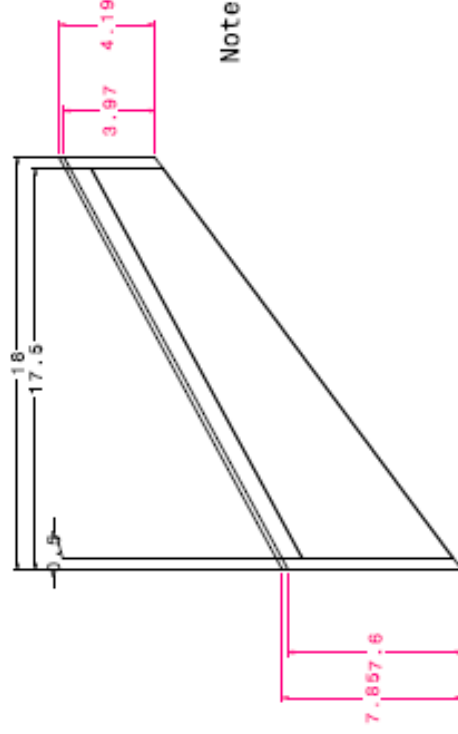
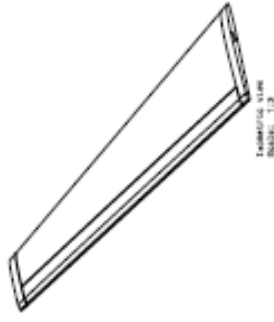
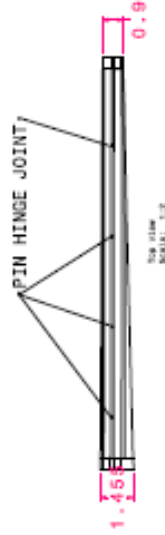


```
front_view[a]
scalar: 1.0
```

Notes:

- 1) ALL PIN AND PIN HINGE JOINTS ARE 1/8" DIAMETER
- 2) PLEASE SEE LEFT FUSELAGE CAT FOR NON-DIMENSIONED SOLID TO SKIN SPACING FOR ADDITIVE MFG.
- 3) ALL INTERNAL CORE DIMENSIONS ARE FROM THE CENTER OF THE FILAMENTS FOR ADDITIVE MFG.

[illegible]

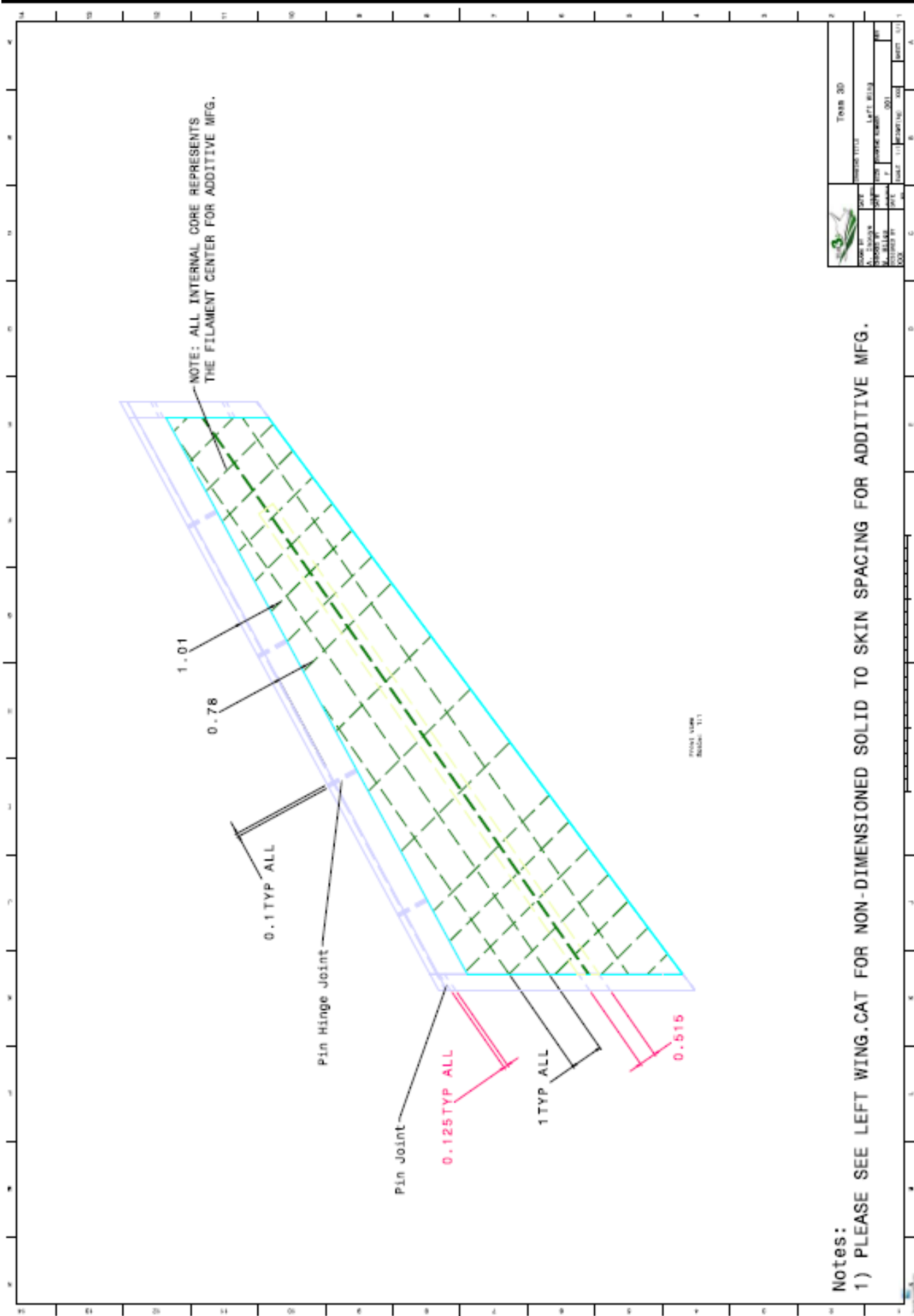


Notes:

1) PLEASE SEE LEFT WING.CAT FOR NON-DIMENSIONED SOLID TO SKIN SPACING FOR ADDITIVE MFG.

		<p>TABLE 30</p>	
<p>PROJECT NAME</p>	<p>PROJECT TITLE</p>	<p>DATE</p>	<p>LEFT WING</p>
<p>DESIGNER</p>	<p>DESIGNER NAME</p>	<p>DATE</p>	<p>DATE</p>
<p>APPROVED BY</p>	<p>APPROVED NAME</p>	<p>DATE</p>	<p>DATE</p>
<p>DATE</p>	<p>DATE</p>	<p>DATE</p>	<p>DATE</p>





Notes:  
 1) PLEASE SEE LEFT WING.CAT FOR NON-DIMENSIONED SOLID TO SKIN SPACING FOR ADDITIVE MFG.